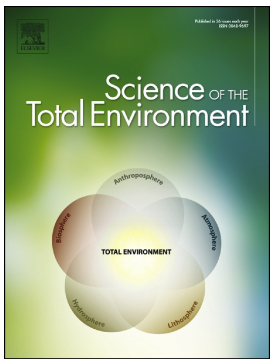

Scaled outdoor experimental studies of urban thermal environment in street canyon models with various aspect ratios and thermal storage

Guanwen Chen, Dongyang Wang, Qun Wang, Yuguo Li, Xuemei Wang, Jian Hang, Peng Gao, Cuiyun Ou, Kai Wang

PII: S0048-9697(20)31660-0

DOI: https://doi.org/10.1016/j.scitotenv.2020.138147

Reference: STOTEN 138147

To appear in: *Science of the Total Environment*

Received date: 15 January 2020

Revised date: 18 March 2020

Accepted date: 21 March 2020

Please cite this article as: G. Chen, D. Wang, Q. Wang, et al., Scaled outdoor experimental studies of urban thermal environment in street canyon models with various aspect ratios and thermal storage, *Science of the Total Environment* (2018), https://doi.org/10.1016/j.scitotenv.2020.138147

To be resubmitted to Science of the Total Environment 2020

Scaled outdoor experimental studies of urban thermal environment in street canyon models with various aspect ratios and thermal storage

Guanwen Chen[1], Dongyang Wang[1], Qun Wang[2], Yuguo Li[2], Xuemei Wang[3], Jian Hang*[1,4], Peng Gao[1], Cuiyun Ou[1], Kai Wang*[2]

[1]School of Atmospheric Sciences, Guangdong Province Key Laboratory for Climate Change and Natural Disaster Studies, Sun Yat-sen University, Guangzhou, P.R. China 510275

[2]Department of Mechanical Engineering, the University of Hong Kong, Pokfulam Road, Hong Kong

[3]Institute for Environmental and Climate Research, Jinan University, Guangzhou, P. R. China

[4]Southern Marine Science and Engineering Guangdong Laboratory(Zhuhai), Zhuhai, China

*Corresponding author: Jian Hang, Kai Wang

Tel: +86-13710248541

E-mail address: hangj3@mail.sysu.edu.cn; kwanghku@connect.hku.hk

Abstract:

Street aspect ratios and urban thermal storage largely determine the thermal environment in cities. By performing scaled outdoor measurements in summer of 2017 in Guangzhou, China, we investigate these impacts on spatial/temporal characteristics of urban thermal environment which are still unclear so far. Two types of street canyon models are investigated, i.e. the 'hollow' model resembling hollow concrete buildings and the 'sand' model consisting of buildings filled with sand attaining much greater thermal storage. For each model, three street aspect ratios (building height/street width, *H/W*=1, 2, 3; *H*=1.2 m) are considered.

The diurnal variations of air-wall surface temperatures are observed and their characteristics are quantified for various cases. The daily average temperature and daily temperature range (*DTR*) of wall temperature vary significantly with different aspect ratios and thermal storage. During the daytime, wider street canyon (*H/W*=1) with less shading area experiences higher temperature than narrower ones (*H/W*=2, 3) as more solar radiation received by wall surfaces. At night, wider street canyon cools down quicker due to stronger upward longwave radiation and night ventilation. For hollow models, *H/W*=1 attains *DTR* of 12.1 ℃, which is 1.2 and 2.1 ℃ larger than that of *H/W*=2, 3. Moreover, the sand models experience smaller *DTR* and a less changing rate of wall temperature than hollow models because larger thermal storage absorbs more heat in the daytime and releases more at night. *DTR* of hollow models with *H/W*=1, 2, 3 is 4.5, 4.6 and 3.8 ℃ greater than sand models respectively. For

both hollow and sand models, wider streets experience a little higher daily average temperature (0.3-0.6 ℃) than narrower ones. Our study provides direct evidence in how man-made urban structures influence urban climate and also suggests the possibility to control outdoor thermal environment by optimize urban morphology and thermal storage.

Keywords: Scaled outdoor measurement of urban climate and health (SOMUCH), Street canyon, Aspect ratio, Thermal storage, Daily temperature cycle, Daily temperature range (*DTR*)

1. Introduction

Due to urbanization, our cities are becoming higher and denser. The increased human-made urban structures have greatly altered the surface energy balance of the urban area, and formed the unique urban climate differing from rural area (Arnfield, 2003; Fernando et al., 2010), such as the relative poorer urban ventilation (Britter and Hanna, 2003; Hang et al., 2015; Chen et al., 2017) and the warmer air/wall temperature than the surrounding rural areas, i.e. urban heat island (Zhao et al., 2014; Oke et al., 1991 and 2017). The urban heat island has been verified to produce a substantial increase of building energy consumption for summer cooling in cities (Fung et al., 2006; Santamouris, 2014; Yang et al., 2015), adverse effects on outdoor thermal comfort (Salata et al., 2017) and public health (Mora et al., 2017), especially during heatwave period (Hass and Ellis, 2019). Thus, understanding the correlations

between human-made urban structures and urban thermal environment is essential for the mitigation of urban heat island and the development of sustainable and healthy urban-built environment.

Urban heat island is mostly resulted from the high thermal capacity of urban materials, reduced greenery and evaporative cooling, the impacts of canyon geometry on radiation capture and weakened urban airflow, as well as the associated anthropogenic heat and pollutant emissions (Arnfield, 2003; Oke et al., 2017). Apart from high albedo material and suitable tree planting (Mackey et al., 2012; Santamouris, 2014; Yan et al., 2018; Chatterjee et al., 2019; Manoli et al., 2019), sustainable urban thermal properties and urban geometrical layouts are also confirmed as effective technique to improve urban ventilation and reduce urban heat island intensities (Grimmond et al., 2010; Zhao et al., 2014; Lai et al., 2019). High thermal capacity of urban surface materials contributes to urban heat island that a larger amount of the incoming solar radiation is stored during the daytime then released at night (Oke et al., 1991 and 2017; Peng et al., 2012). Urban morphology influences not only urban airflows and pollutant dispersion (Lin et al., 2014; Chen et al., 2017; Scungio et al., 2018; Yuan et al., 2019; Zhang et al., 2019) but also the amount of both incoming and outgoing radiation (Oke et al., 1991 and 2017; Arnfield, 2003; Harman et al., 2004). As depicted in Fig. 1a, from shallow to deep street canyons, it tends to change both ventilation and radiation processes, which results in a non-linear relationship between urban geometrical morphologies and urban thermal environment due to the counteracting processes including cooling by convection, the shading and

trapping effects of solar radiation (Oke, 1988; Zhao et al., 2014; Song and Wang, 2015). Further investigations are still required to distinguish the impacts of urban morphologies and building thermal capacities on urban thermal environment.

The idealized two-dimensional (2D) street canyon means an infinitely long street surrounded by buildings on both sides with a perpendicular approaching wind to street axis. As reviewed in the literature (e.g. Zhang et al., 2018), it has been commonly employed to study and clarify the basic governing mechanisms of many phenomena in urban areas, due to its simple but fundamental geometry to synthesize the physical processes (e.g. Gu et al., 2011; Dallman et al., 2014; Hang et al., 2017).

Numerical modelling is one of the effective approaches to investigate the influence of urban morphologies on urban airflow, pollutant dispersion and thermal environment in street canyons. Many previous numerical simulations have investigated the impacts of street aspect ratios (Hang et al., 2017; Zhang et al., 2019), urban vegetation (Gromke et al., 2008; Hong and Lin, 2015), buoyancy force induced by wall heating and solar heating (Allegrini et al., 2014; Li et al., 2016; Lin et al., 2016) etc. However, high-quality experimental data on urban thermal environment are necessary and still rare to validate the numerical accuracy and further improve the numerical model.

Monitoring and full-scale field experiments in realistic urban environment are essential to provide direct evidence of urban warming and analyze the characteristics of urban heat island (Grimmond et al., 2010). A number of full-scale field experiments in real street canyons have been carried out to study the characteristics of

urban thermal environment. Nakamura and Oke (1988) observed the characteristics of air-wall temperature under different stability conditions in an east-west street canyon (*H/W*=1.06). The maximum surface-air temperature differences can reach around 12-14 ℃ during the experiment. Santamouris et al. (1999) conducted a field experiment to investigate the thermal characteristics in a deep (*H/W*=2.5) street canyon with NW-SE orientation under hot weather conditions. The surface temperature difference between two opposite building walls can reach up to 19 ℃ due to different absorption of solar radiation. Louka et al. (2002) investigated the thermal effects on the airflow when the windward side is heated (*H/W*=1.4). A thin thermal layer was revealed within only few centimeters from the heated wall, which indicates thermal effects were only significant very close to the wall. Johansson (2006) compared outdoor thermal comfort between an extremely deep (*H/W*=9.7) and a shallow (*H/W*=0.6) street canyon in Fez, Morocco. During summer, the deep canyon exhibited a better comfortable level due to better solar shading effect. However, during winter, the shallow canyon is more comfortable because of adequate solar access. Niachou et al. (2008) studied air and surface temperature distribution in a street canyon with the aspect ratio (*H/W*) of 1.7, under hot weather conditions in Athens. No significant variations in the vertical distribution of air temperature was observed in the centre of canyon. Giannopoulou et al. (2010) performed comparative and simultaneous outdoor measurements to investigate the effect of urban morphologies (*H*=21 m, *H/W*=1.7, 2.1 and 3) on the night thermal regime and they found that street canyons with higher aspect ratios experienced lower cooling rates.

All these full-scale experimental studies help understanding the influencing mechanisms of urban thermal environment. However, their spatial and temporal resolutions are usually limited. Moreover, these full-scale field experiments mostly emphasized case studies which locate in different cities under various meteorological conditions. Nevertheless, high-quality parametric observational studies in realistic street canyons have several challenges. Firstly, it is not easy to control urban geometries and thermal properties (building materials and surface colors etc.) in real cities. Secondly, spatial characteristics of urban geometries and thermal properties are heterogeneous and complicated (Yang and Li, 2009; Stewart and Oke, 2012). Such complexity may reduce the representativeness of the spatial coverage and cause data uncertainties and errors in field measurements. Finally, instrumentation installation is also challenging at different heights far from pedestrian levels and building surfaces due to cost, logistics and permit issues (Eliasson et al., 2006; Offerle et al., 2007; Fan et al., 2016). Therefore, high-quality parametric studies of urban thermal environment in such full-scale outdoor measurement are essential, but usually difficult. The impacts of different aspect ratios and thermal storage on urban thermal environment under the same meteorological conditions have been rarely investigated by parametric full-scale outdoor experiments.

Among scaled studies, wind tunnel experiments provide the good approach to control urban geometrical parameters, that have been widely conducted to study the influence of urban layouts and uniform wall heating on characteristic of urban airflow and pollutant dispersion (Uehara et al., 2000; Allegrini et al., 2013; Cui et al., 2016；

Chen et al., 2017). However, the diurnal cycles of solar radiation and building heat storage are hardly realized in wind tunnel. Furthermore, water tank experiments can effectively investigate the interactions of dynamic force and buoyancy force in urban airflow (Fan et al., 2018a and 2018b) but they cannot simulate the daily cycle of urban thermal environment with heat storage and radiation processes either. Scaled outdoor measurements are verified as the good option to perform parametric experimental study of flow and urban thermal environment. Not only building parameters can be easily controlled to test the influence of various urban configurations under the same meteorological condition, thermodynamic similarity requirements can also be satisfied (Kanda et al., 2005; Kanda, 2006; Kawai and Kanda, 2010a). Aida (1982) used cubic concrete blocks (0.15 m width) with same surface quality to examine the effect of the surface irregularity on urban albedo. It is found that the albedo decreases as the surface irregularity increases. The MUST experiment (Yee and Biltoft, 2004) adopted ship containers to build a scaled 3D ideal city of sparse building clusters (H=2.54 m, plan area density λ_p=0.096, frontal area density λ_f=0.1), which mainly used to study the characteristics of urban turbulence and pollutant dispersion. The COSMO field experiments used 512 uniform cubic concrete models (H=1.5 m, λ_p=0.25, λ_f=0.25) to mock urban area and study the basic features of the surface energy balance through a long-term measurement (Kawai and Kanda, 2010a and 2010b). In addition, Park et al. (2012) studied the effect of urban vegetation and Syafii et al. (2017) examined the influence of various water body configurations on the urban thermal environment in COSMO. Wang et al. (2018)

investigated the effect of urban morphology on daily temperature cycle in the Stone Forest. The literature (Pearlmutter et al., 2006 and 2007a) used an open-air scaled model to quantify the influence of 2D urban geometry (H=0.2 and 0.4 m; H/W=0.33, 0.66, 1, 2) on pedestrian energy exchange under typical hot-arid summer conditions. Dallman et al. (2014) constructed a 2D street canyon with ship containers (H=2.5 m, H/W=2/3) to measure the wind or heat-dominated flow characteristics and they defined a buoyancy factor to distinguish the dominant mechanism. Such scaled outdoor measurements can also provide high-quality parametric experimental data for numerical simulation and theoretical modeling (Silva et al., 2009; Toparlar et al., 2015; Yang and Li, 2015; Meroney et al., 2016; Yang et al., 2017; Athamena et al., 2018a and 2018b; Liang et al., 2018; Antoniou et al., 2019).

This paper aims to present a scaled outdoor model which mimic 2D street canyon, and investigate the impact of urban thermal storage (i.e. hollow model and sand model) and typical aspect ratios (H=1.2 m, H/W=1, 2, 3) on the characteristics of turbulence and urban thermal environment, which are still rare so far. The diurnal cycles of urban air and wall temperature are first characterized here. Direct evidence in how man-made urban structures influence urban thermal environment is revealed. And the high-quality experimental data can be adopted for validation of numerical and theoretical models in future urban climate studies.

2. Methodology

2.1 Experimental setup

The scaled outdoor field experiment was conducted in the campus of Sun Yat-sen University, locating in the suburb of Guangzhou, P.R. China (23°4' N, 113°23' E). We chose an experimental field with impermeable concrete floor, and the distance to the surrounding buildings is sufficiently far (as shown in Fig. 1a-b) to reduce the impact of surrounding buildings on local wind in this outdoor platform. In this study, the idealized urban models are simplified consisting of hollow concrete cubic models (0.5 m$\times$0.5 m$\times$1.2 m) with 0.015 m thickness and the constant building height (H=1.2 m). To study the impact of heat storage, two types of urban configurations were used here, named as the 'hollow' model and the 'sand' model. The 'hollow' model resembles the hollow buildings with less thermal storage capacity while the 'sand' model is made up of concrete building models filled with sand to produce much greater heat capacity. The dimensionless parameter τ can be used to evaluate the effect of thermal inertia (Yam et al., 2003). The larger the parameter τ, the stronger the heat storage capacity. For instance, as H/W=1, τ of hollow model is around 87.3 s, while for sand model, τ is about 1224 s (Wang et al., 2017). In order to mimic canyons with different morphologies, different street widths were set, i.e. W=1.2 m, 0.6 m, or 0.4 m, and the aspect ratio H/W=1, 2, 3 accordingly. Each aspect ratio contains six street canyons and each row of street canyon consists of 25 building models, with street length of 12.5 m (L>10 H). In total, there were 2000 concrete building models, forming 40-row north-south street canyons for each urban model (Fig. 1a-b). Furthermore, the detailed definitions of street canyon surfaces are shown in Fig. 1c. The experimental period is May-June, 2017, and this paper focuses on typical weather conditions in hot summer

of a subtropical region.

During the experimental period, ultrasonic anemometers (Gill WindMaster), ibuttons, thermocouples and weather stations were used to measure the three velocity components (U_x, U_y, U_z) and turbulence, air temperature, surface temperature and background atmospheric condition respectively. For street canyons with different aspect ratios and thermal storage, measurements were performed simultaneously and the placements of all the instruments were similar. The detailed specifications and configurations of the instrumentations used in the present study are given in Table 1, Fig. 1b (top view) and Fig. 2a-c (side view).

Fig. 2a shows that twenty-two three-dimensional (3D) sonic anemometers (Gill WindMaster) were horizontally instrumented at five different heights (z=0.3 m, 0.6 m, 0.9 m, 1.44 m, 2.4 m) along the centerline of the canyon (H/W=2, 3; H=1.2 m), to measure the detailed 3D velocity and turbulence within and above street canyons. Due to the limited numbers of instrument, only one sonic anemometer was installed at z=0.3 m in the centerline of the widest street canyon (H/W=1).

Thirty temperature sensors (ibutton, DS1922L) with radiation shield were used to measure air temperature at the interval of 10 minutes. As shown in Fig. 2b, five of them were placed at different heights (z=0.1 m, 0.3 m, 0.6 m, 0.9 m, 1.44 m) along the centerline of each street canyon. The measurement range and accuracy of this sensor were -40 to 85 ℃ and ± 0.5 ℃.

As depicted in Fig. 2b, 246 thermocouples (Type K) were mounted on the vertical walls, the ground and roof surfaces to measure the surface temperatures of all

surfaces in the canopy. In addition, the thermocouples were also arranged inside the concrete model to measure the internal air or sand temperature within buildings and placed in the center of street canyon to measure street air temperature. These temperature data were recorded continuously by Agilent 34972A data loggers at intervals of 1 minute. The positions of the thermocouples on the wall and inside building were the same for all street canyons (z=0.3 m, 0.6 m, 0.9 m, 1.1 m). Five thermocouples were placed evenly at the centreline of the ground surface at the north-south direction. Four thermocouples were placed for air temperature in the center of the canyon at different heights (z=0.1 m, 0.3 m, 0.6 m, 1.44 m) and four thermocouples were evenly arranged on the roof surface.

In order to obtain more comprehensive information of building surface temperature, two infrared cameras (R500) were applied to measure the temperature at wall surfaces. The spatial resolution of R500 infrared camera is 640 × 480 with the temperature measurement accuracy at ± 1 ℃. The temperature measurement range and the field of view are -40 to 500 ℃ and 32° × 24°. The infrared camera measurements require the input parameter emissivity, which is affected by the angle between the surface and the camera. To minimize the error induced by the angle, the direction of the infrared camera is preferably perpendicular to the wall surface. For this purpose, we adopted an up-down controlling system to fix the exact vertical location of the infrared camera and take multiple images in the vertical direction by infrared camera to measure the entire wall surface temperature inside the street canyon (Fig. 2c). We took infrared images every hour during selected sunny days

(June 24th -27th, 2017) to capture the detailed vertical variation of the wall temperature.

As depicted in Fig. 1a-b, two weather stations (RainWise PortLog) were put in the central of the experiment site to measure the background air temperature (T_b), barometric pressure, solar radiation, rainfall, wind direction and wind speed. The monitoring time interval was set as 10 minutes. The sensors of the weather station were set at a height of 2.4 m (i.e. 2*H*) above the ground.

In the following analysis, the impacts of two types of building heat storage (hollow and sand models) and three street aspect ratios (*H/W*=1, 2, 3) on diurnal cycle characteristics of wall and air temperature will be characterized. For temperature analysis, T means the original temperature data, $\overline{T}$ represents temporal averaged temperature for 10 minutes or one day/several days (if not specified, the temperature data will be averaged for 10 minutes) and <T> denotes spatially-averaged temperature. <$\overline{T}$> denotes spatially-averaged values of temporal averaged temperature (i.e. $\overline{T}$ at building walls <$\overline{T}_{wall}$>, building roof <$\overline{T}_{roof}$>, ground <$\overline{T}_{ground}$>, and street air <$\overline{T}_{air}$> at various points).

2.2 Similarity analysis

To mimic real world, scale modeling requires both geometrical similarity (not fundamentally difficult) and dynamical similarity (much more difficult) between the scaled model and the real world (Kanda, 2006; Oke et al., 2017; Wang et al., 2018).

The dynamical similarity requires the similarities of air flow, radiation and thermal inertia.

To get a similar flow field compared to the real world, Reynolds number (Lu et al., 1997; Allegrini et al., 2013) can be used to the similarity criterion:

$$\mathrm{Re} = \frac{U_{ref} H}{v} \tag{1}$$

where U_{ref} is the background reference velocity, H is the street canyon height and v is the kinematic viscosity.

Table 2 summarizes typical Reynolds numbers (Re) with characteristic reference velocity in our study period (U_{ref}=0.1 m/s, 0.5 m/s and 2 m/s; H=1.2 m). Although it is difficult to reach the same Reynolds number in scaled model compared to the full-scale realistic street canyon, the flow structure is similar as long as the Reynolds number independence requirement is satisfied for which the critical Reynolds number is about 11000, i.e. Re>>11000 (Snyder, 1972). During the scaled experiment period, the Reynolds numbers are 41096 at characteristic U_{ref}=0.5 m/s and 164384 at typical U_{ref}=2 m/s (here H=1.2 m, see Table 2) which are sufficiently large to ensure Reynolds number independence (Snyder, 1972).

Wind-driven dynamic force and thermal buoyancy force are two main driving forces in urban ventilation airflow and pollutant dispersion. The bulk Richardson number (Ri_b) can be used to characterize the relative importance of buoyancy force and wind-driven dynamic force on turbulent flow (Xie et al., 2005; Richards et al., 2006), which is defined as below:

$$Ri_b = \frac{\beta g H(T_w - T_{ref})}{U_{ref}^2} = \frac{gH\Delta T / T_{ref}}{U_{ref}^2} \quad (2)$$

where U_{ref} is the background reference velocity, T_{ref} is the reference air temperature and $\beta = 1/T_{\mathrm{ref}}$ is the thermal expansion coefficient, g is the gravitational acceleration, H is the street canyon height, T_w is the canyon surface temperature, and ΔT(T_w-T_{ref}) is the temperature difference between canyon surface and background air.

It is well known that three situations can be classified (Xie et al., 2005; Richards et al., 2006): If Ri_b>>1 (i.e. much greater than one), thermal buoyancy force dominates urban airflow; If Ri_b<<1 (i.e. much smaller than one), wind-driven dynamic force dominates and buoyancy force can be disregarded; If Ri_b is in order of 1, both forces are significant and interact in determining urban turbulence.

Table 2 lists the further calculated bulk Richardson number (Ri_b) with typical reference values in our study period (U_{ref}=0.1 m/s, 0.5 m/s and 2 m/s; H=1.2 m, T_{ref}=300 K, ΔT =T_w-T_{ref}=10 K). The urban airflow that can be simulated in our scaled model (H=1.2 m) mainly corresponds to the situation when wind-driven dynamic force dominates (e.g. U_{ref}=2 m/s, Re=164384, Ri_b=0.1<<1) or both forces cannot be neglected with important interactions (e.g. U_{ref}=0.5 m/s, Re=41096, Ri_b=1.57~1). The case with buoyancy force dominated urban airflow (Ri_b>>1) in our scaled model (H=1.2 m) seldom occurs if only the background wind speed is smaller (e.g. Ri_b=39.2 as U_{ref}~0.1 m/s and ΔT =T_w-T_{ref}=10 K). However, in this situation, it is difficult to attain a sufficiently large Re (e.g. Re=8219 in Table 2) and cannot satisfy Reynolds number independence requirement (i.e. Re>>11000) (Snyder, 1972). Thus the buoyancy-force-dominated urban airflow (Ri_b>>1) seldom appears in the present

scaled street canyons. And it is worth noting that, for the case with both thermal buoyancy and wind-driven dynamic forces cannot be neglected (Ri_b~1), wind-tunnel-scale model (Kovar-Panskus et al., 2002; Allegrini et al., 2013) requires a larger temperature difference (~100 ℃), while our scaled model only needs a normal temperature difference (~10 ℃).

To achieve similarities of radiation and thermal inertial, our experiment uses concrete materials to match the thermal properties of real urban city. The detailed physical properties of materials used in the experiment are shown in Table 3 and the calculated thermal admittance μ (the square root of the product of the material's thermal conductivity λ and volumetric heat capacity s) of concrete material (μ =1761 $Jm^{-2}s^{-1/2}K^{-1}$) used in our experiment falls within the range (μ =1200-2100 $Jm^{-2}s^{-1/2}K^{-1}$) of typical urban materials (Oke, 1981). The similarity of radiation and thermal inertia in such scaled models (H~1 m) are also discussed in the literature (Aida, 1982; Kanda et al., 2005; Kanda, 2006; Pearlmutter et al., 2005 and 2007b) which is similar with present study.

3. Results and discussions

3.1 A typical diurnal cycle of urban thermal environment

We measured spatial and temporal wall temperature at least three consecutive days by two infrared cameras and a number of thermocouples simultaneously. As an example, Fig. 3a displays the daily cycle characteristic of wall temperature (T_{wall}) captured by infrared camera in one typical day (June 26th, 2017). It is obvious that the

wall begins to be heated up in the morning, and reaches the highest temperature in the mid-afternoon (about 15:00 to 16:00), then it cools down from the late afternoon and at night due to longwave radiative and convective cooling. Similar daily cycle phenomena are also observed by $\bar{T}_{wall}$ that measured by thermocouples (Fig. 3b).

Diurnal cycle of wall and air temperature at various height

In order to study the vertical temperature profiles within the canopy, the wall temperature $\bar{T}_{wall}$ were also measured by thermocouples at four heights of z=0.3 m, 0.6 m, 0.9 m, 1.1 m (H=1.2 m). Fig. 3b is the diurnal profiles of $\bar{T}_{wall}$ at different levels on June 26th, 2017 (the same day with Fig. 3a). It shows that the upper levels (e.g. z=1.1 m and 0.9 m) experience higher $\bar{T}_{wall}$ than the low levels (e.g. z=0.6 m and 0.3 m) in the daytime as upper canopy receives more solar radiation with less solar shading than that near the ground. However, it shows the opposite trend at night, i.e. the upper levels tend to be cooled down faster induced by stronger ventilation and longwave radiation. The distribution of the air temperature $\bar{T}_{air}$ at various heights measured by ibuttons in the centre of street canyon is shown in Fig. 3c. The relatively uniform $\bar{T}_{air}$ distribution at various heights suggest that turbulent flows in street canyons significantly enhance the turbulent mixing of air and energy. This is consistent with the observations in realistic street canyon of Niachou et al. (2008).

Comparison between thermocouple data and IR results

We further quantified the difference in the measured wall temperature between

thermocouple and infrared camera, to verify whether measuring spatially-averaged wall temperature at selected points by thermocouples be representative of the entire wall temperature. Fig. 3d displays the example of diurnal $<T_{wall}>$ profiles of the south wall of hollow model (*H/W*=3) that measured by both thermocouples and infrared camera on June 26th 2017. Obviously both $<T_{wall}>$ averaged at four heights by thermocouples and averaged at the entire wall surface by infrared camera show similar characteristics of diurnal cycle of wall temperature. Furthermore, as shown in Table 4, the mean absolute error (MAE) between infrared camera and thermocouple is 0.7 ℃, the root mean squared error (RMSE) is 0.87 ℃, suggesting a good consistency between two measurements. Considering the accuracy of thermocouples ($\pm$0.3 ℃) and R500 infrared camera ($\pm$1 ℃), it confirms the measurements by thermocouples at current selected heights can be used to represent the $<T_{wall}>$ at the entire wall surface.

Comparison of diurnal cycle of $<\overline{T}_{wall}>$, $<\overline{T}_{ground}>$, $<\overline{T}_{roof}>$, $<\overline{T}_{air}>$ and background $\overline{T}_b$ at z=2H

Furthermore, as depicted in Fig. 3e, various temperature measurements during three consecutive days (May 18th-20th, 2017), including the diurnal variation of spatially-averaged roof temperature $<\overline{T}_{roof}>$ at eight points, spatially-averaged wall temperature $<\overline{T}_{wall}>$ at eight points of building walls, spatially-averaged ground temperature $<\overline{T}_{ground}>$ at five points, spatially-averaged air temperature $<\overline{T}_{air}>$ at three points (inside street canyon) and the background air temperature ($\overline{T}_b$) at the

height of 2*H* (above street canyon) of hollow model (*H/W*=1) are compared here to have a holistic view of thermal environment considered in this study. Obviously, all surfaces show prominent diurnal cycle characteristics and much higher than the air temperature in the daytime and closer to the air temperature during the night. During the daytime, temperature is dominated by the solar radiation. The solar radiation reaching at the surface heats up the surface temperature first and the air temperature increases accordingly through the convective heat transfer between the surface and the air. Thus, although the maximum surface temperature varies in three different days due to the various weather conditions and net solar radiation, $<\bar{T}_{roof}>$ is the highest as there is no solar shading and more solar radiation captured at building roof. $<\bar{T}_{roof}>$, $<\bar{T}_{wall}>$ and $<\bar{T}_{ground}>$ are all much higher than $<\bar{T}_{air}>$ and $<\bar{T}_{air}>$ is higher than $\bar{T}_b$, verifying clearly that street wall changes the energy processes and results in the hotter air inside street canyon than the background air ($\bar{T}_b$). The results show the maximum surface-air temperature difference is around 10-12 ℃ for the building roof, about 6-7 ℃ for the ground and approximately 5-6 ℃ for the building wall. It is interesting to point out that the maximum surface temperature occurs in the afternoon (around 15:00 pm) in all three days, which is verifying the energy lag phenomena (Wang et al., 2018). At night, the differences between various temperature are much smaller and close to the background temperature due to nocturnal cooling. $<\bar{T}_{roof}>$ is the lowest among all three surfaces (roof, ground, wall) and lower than the air temperature. $<\bar{T}_{ground}>$ is the highest among all the surfaces. The building roof cools down the quickest by the most efficient ventilation and longwave radiative

cooling (greatest sky view factor), however the ground is of the weakest wind flow and the smallest sky view factor which results in the slowest temperature reduction rate.

3.2 Impact of street-wall orientation and weather conditions on $\bar{T}_{wall}$ and $<\bar{T}_{wall}>$

As the surface temperature is determined by the solar radiation reaching at the surface, the street-wall orientation and weather condition are important factor in affecting the wall temperature. Fig. 4a-b display the hourly infrared images of south wall and north wall of the hollow model (*H/W*=1) on June 26th, 2017. During the daytime (Fig. 4a), the surface temperature of the south wall is always higher than that of the north wall as the south wall receives more direct shortwave radiation while the north wall gets more shading area. Besides, the temperature difference between north wall and south wall increases when the solar radiation becomes stronger. However, during the night (Fig. 4b), the temperature difference between north wall and south wall is negligible because of the absence of solar radiation and cooling processes is similar between two walls.

Fig. 4c-d further demonstrate the impact of weather condition on wall surface temperature. The diurnal variation of single-point wall temperature $\bar{T}_{wall}$ (z=0.6 m, 1 point for north wall, 1 point for south wall) and spatially-averaged temperature $<\bar{T}_{wall}>$ (4 points for north wall, 4 points for south wall and 8 points for both wall) of hollow model (*H/W*=1) are compared between a sunny day and cloudy day. On one

hand, during the daytime of the sunny day (Fig. 4c), the wall temperature has increased significantly along with the enhancement of solar radiation. Thus, the single peak of wall temperature appears. However, on cloudy day (Fig. 4d), obviously the single peak of wall temperature diurnal cycle does not exist anymore due to the variations of clouds and solar radiation. The comparison suggests again that the weather condition and solar radiation have a significant effect on wall temperature. On the other hand, the diurnal variations of single point temperature $\bar{T}_{wall}$ and $<\bar{T}_{wall}>$ are very similar between north wall and south wall (Fig. 4c-d). Thus, in order to present more representative information about thermal environment, the spatially-averaged temperature will mainly be shown in the following analysis.

3.3 Impact of aspect ratio on urban thermal environment

Aspect ratio is an important parameter indicating the urban form and compactness, which influences the urban thermal environment by changing both radiation and air flow. Fig. 5 displays some example daily cycles of wall temperature that measured by infrared camera (Fig. 5a) and thermocouples (Fig. 5b) in street canyons with three different aspect ratios (*H/W*=1, 2, 3).

As depicted in Fig. 5a, obviously in the morning, deeper and narrower street canyon (*H/W*=2, 3) is cooler since its sky view factor is smaller and the shading effect is larger, especially the lower level of deep street canyons attain much less radiation. Wider street canyon (*H/W*=1) gains more solar radiation and warms up faster in the morning. Overall, the wider the street canyon, the higher the wall temperature in the

daytime.

In addition, Fig. 5b shows diurnal variation of wall temperature in different street canyons. During the daytime, the temperature difference between wide (*H/W*=1) and narrow (*H/W*=2, 3) street canyon is increasing, and the maximum difference can reach up to 2.6 ℃ around the noon time. However, at night, wider street canyon (*H/W*=1) cools down quicker than the narrower street canyons (*H/W*=2, 3) because of the better ventilation and the quicker longwave radiative cooling. Besides, the temperature difference between wider (*H/W*=1) and narrower (*H/W*=2, 3) street canyon becomes smaller during the night, which is less than 0.5 ℃.

3.4 Impact of thermal storage on urban thermal environment

Building thermal storage is another key parameter influencing urban thermal environment. Fig. 6a-c show the infrared images of the canyons with three different aspect ratios (*H/W*=1, 2, 3) between hollow model and sand model measured on June 26th, 2017. It verifies that, during the daytime, the hollow model always warms up faster than the sand model, but at night the sand model is hotter because buildings with larger storage tend to store more heat in the daytime which keeps the building to be warmer during night. In addition, the difference in nighttime wall temperature between hollow model and sand model becomes more obvious when the aspect ratio is larger.

Such findings are also confirmed by the thermocouple measurements under different conditions. Fig. 6d-e display the diurnal profile of $<\bar{T}_{wall}>$ at eight points of

hollow and sand model (*H/W*=1) measured by thermocouples under different weather condition. During the daytime on sunny day (Fig. 6d), $<\bar{T}_{wall}>$ of hollow model is higher than the sand model. Furthermore, there is a temperature phase lag between the hollow model and sand model, i.e. the maximum $<\bar{T}_{wall}>$ of hollow model occurs earlier (around 13:50) than the sand model (about 14:40, 1 hour time lag). What's more, the difference between the maximum and minimum temperature of hollow model (i.e. daily temperature range, *DTR*) is significantly larger than the sand model. *DTR* of $<\bar{T}_{wall}>$ of hollow model is 14.9 ℃ while the sand model is 9.5 ℃.

In addition, Fig. 6e shows the diurnal variation of $<\bar{T}_{wall}>$ on a cloudy day. As discussed before, the single peak of diurnal wall temperature does not exist anymore on the cloudy day, no significant temperature phase difference is observed in this case. However, even in the cloudy weather condition, similar findings can be found that the sand model experiences lower wall temperature in the daytime but attains higher wall temperature at night than the hollow model, though the difference in *DTR* of $<\bar{T}_{wall}>$ between hollow model (10.0 ℃) and sand model (8.6 ℃) is much smaller than that in a sunny day.

In general, the comparison confirms that, due to the smaller heat capacity and thermal mass, the hollow model experiences less heat storage, faster response to the change of radiation and is easier to reach a peak temperature in the daytime, meanwhile also easier to cool down at night.

3.5 Vertical distribution of T_{wall} at lower and upper levels as *H/W*=1, 2, 3

The vertical distribution of wall temperatures are further investigated by comparing the wall temperature (T_{wall}) distribution of the lower and upper levels. Fig. 7a-b show the boxplots of wall temperature (T_{wall}) of the lower level (z=0.3 m) and upper level (z=1.1 m) on both north and south facades of hollow model with different aspect ratios (H/W=1, 2, 3), during the daytime (07:00-20:00) and night (20:00-07:00) period. Data were selected from the 7 days with valid measurements and no rainfall between May 11th-June 9th, 2017. The boxplot demonstrates the distribution of the temperature data, including the maximum, 75th percentile, average, median, 25th percentile and minimum values. Here, we mainly focus on temporal averaged wall temperature ($\bar{T}_{wall}$, which is the mean value of the corresponding selected data) and wall temperature range (T_{TR}, which is calculated as the difference between maximum and minimum wall temperature of the corresponding selected data) during the daytime and at night respectively.

The upper level receives more solar radiation in the daytime and the maximum wall temperature is higher. As displayed in Fig. 7a, during the daytime, for the same aspect ratio and wall orientation, both $\bar{T}_{wall}$ and T_{TR} at the upper level (z=1.1 m) are always higher than those of the lower level (z=0.3 m), especially in south wall. The maximum T_{TR} is up to 20.4 ℃, which occurs in upper level of south wall. The aspect ratio also affects the vertical temperature distribution as its impact on the radiation processes. For the upper level (z=1.1 m, north and south wall), the differences of $\bar{T}_{wall}$ between three different aspect ratios are small, as well as T_{TR}. The maximum $\Delta\bar{T}_{wall}$ and ΔT_{TR} between different canopies are 0.9 ℃ and 2.0 ℃,

respectively. However, for lower level (z=0.3 m, north and south wall), the differences in $\bar{T}_{wall}$ between three different aspect ratios are much greater, as well as the differences in T_{TR}. The maximum $\Delta\bar{T}_{wall}$ and ΔT_{TR} are 2.0 ℃ and 3.9 ℃, respectively. This indicates that during the daytime, street aspect ratio has more significant impact on the $\bar{T}_{wall}$ and T_{TR} at the lower levels (receive less solar radiation with more solar shading) than the upper levels (receive more solar radiation).

The lower level loses less longwave radiation at night and the minimum wall temperature is higher. As depicted in Fig. 7b, at night, due to the absence of solar radiation, the corresponding $\bar{T}_{wall}$ and T_{TR} of the upper level (z=1.1 m) and lower level (z=0.3 m) at night were both smaller than those during the daytime. $\bar{T}_{wall}$ at the lower level is higher than the upper level due to the smaller sky view factor and less longwave radiative cooling in the lower level. The smaller wind speeds near the ground level may also play a role. In addition, T_{TR} of lower level is smaller than the upper level. The latter experiences larger temperature range due to better ventilation and greater radiation heat transfer in the upper level. Moreover, for both lower and upper levels, the differences in $\bar{T}_{wall}$ between three different aspect ratios are small, as well as T_{TR}. The maximum $\Delta\bar{T}_{wall}$ and ΔT_{TR} of upper level are 0.4 ℃ and 0.5 ℃, respectively. Besides, the maximum $\Delta\bar{T}_{wall}$ and ΔT_{TR} of lower level are 0.5 ℃ and 0.8 ℃, respectively. This reveals that during the night, street aspect ratio has less impact on the $\bar{T}_{wall}$ and T_{TR} for both lower and upper levels.

3.6 Quantitative as well as overall effects of aspect ratio and thermal storage

Analysis of hot and cold area proportion from infrared temperature

The advantage of infrared camera is that we can measure the surface temperature of the entire wall. In our experiment, we used infrared cameras to measure wall temperature at the same height in terms of different thermal capacity (hollow and sand model), aspect ratios (*H/W*=1, 2, 3) and wall orientation (north and south wall). Based on the measurements, we can quantify the effects of these factors on wall temperature, by calculating the hot and cold area proportion of the wall after a temperature threshold is defined. The temperature threshold for hot area is set as 35 ℃, so the proportion of hot area represents the percentage of wall area with temperature over 35 ℃ to the total wall area. When the hot area proportion is 0, it means no area of the wall is exceeding 35 ℃ at that time. When the hot area proportion is 100%, it represents all the wall surface exceeds 35 ℃ at that time. The cold area proportion is similar, but the threshold is set to 28 ℃ and it shows the proportion of the wall surface with temperature lower than this threshold.

Fig. 8a-d display the hot and cold area proportion of the wall temperature during the day, with different heat capacity (hollow and sand model), aspect ratios (*H/W*=1, 2, 3) and wall orientation (south and north wall). The data were measured by infrared camera on June 26th, 2017.

First, we take the *H/W*=1 sand model as an example to show the diurnal variation of hot and cold area proportion of the wall temperature (Fig. 8a). For hot area proportion, the wall temperature larger than 35 ℃ in the day is appeared

approximately from 11:00 to 18:00. The wall absorbs heat and surface temperature rises after receiving the solar radiation. With the enhancement of the solar radiation, 11.5% of the wall surface area is higher than 35 ℃ at 11:00. After 13:00, with the accumulation of heat, the hot area proportion continues increasing, more than 90% of the wall temperature exceeds 35 ℃ and this phenomenon lasts until 18:00. For cold area proportion, the wall surface area lower than 28 ℃ is appeared approximately from 00:00 to 07:00. The wall releases the heat due to the decrease of solar radiation, mainly from longwave radiation and ventilation. After sunset, the wall takes the time to drop to 28 ℃. It shows 29.2% of the wall surface area is lower than 28 ℃ at 00:00 and reaches 81.5% at 04:00. The heat transfer process at night is different from the daytime. Solar radiation is of the primary energy source for the wall to heat up during the daytime, which can keep the wall warming. However, the factors that determine the nocturnal cooling including the complex longwave radiative transfer between different walls, ground and sky, and ventilation from both convection and advection of heat. All these processes are strongly correlated with the canopy morphology. In order to investigate the effect of other factors (aspect ratio, building thermal capacity and wall orientation) on hot and cold area proportion, we compare the analyses of hot area proportion at four different hours (08:00, 12:00, 14:00, 16:00) and cold area proportion at four different moments (22:00, 00:00, 02:00, 04:00).

As displayed in Fig. 8b, we compare the hot and cold area proportion of wall temperature (sand model, south wall) under different aspect ratios (H/W=1, 2, 3). At 08:00, no wall surface area with three kinds of aspect ratios (H/W=1, 2, 3) exceeds 35

℃. At 12:00, the hot area proportion of the wider street (*H/W*=1) is the largest, which reaches up to 65.6%, while the narrower street for the aspect ratio *H/W*=2, 3 are 6.7%, 24.6%, respectively. Similar phenomena can be observed in the other two moments (14:00 and 16:00). In addition, all the wall surface temperature are higher than 35 ℃ for wider street (*H/W*=1) at 16:00. For cold area proportion, at 22:00, the wall temperatures of three aspect ratios (*H/W*=1, 2, 3) all are higher than 28 ℃. At the rest of moments (00:00, 02:00, 04:00), wider street (*H/W*=1) shows more surface area below 28 ℃ than narrower street (*H/W*=2, 3). It shows the greater longwave radiation and better ventilation because of the bigger sky view factor in the wider street.

The hot and cold area proportion of the wall temperature (*H/W*=3, south wall) under different thermal capacity (hollow and sand model) are described in Fig. 8c. For hot area proportion (at moments 12:00, 14:00, and 16:00), we can find that hollow model shows more surface area higher than 35 ℃ due to the smaller heat capacity. The sand model with larger heat capacity is possessed of the slower temperature change rate. The wall of the sand model needs more time to heat up during the daytime. The cold area proportion at night (02:00 and 04:00) of sand model displays less data lower than 28 ℃. At 04:00, 99% of wall surface area of hollow model is lower than 28 ℃ while none of sand model does. The wall of the sand model also needs more time to cool down during the night.

Fig. 8d shows the example of the hot and cold area proportion of the wall surface temperature (hollow model, *H/W*=1) under different orientations (north and south

wall). South wall begins to receive solar radiation earlier in the morning and absorbs more radiation during the daytime. At 8:00 (the morning), the proportion of hot area on the south wall reaches up to 57.3%, while the north wall is only 0.3%. After that, as the solar elevation angle increases, the difference in the hot area proportion between the south wall and north wall decreases. The difference in proportion of cold area between the south and north wall is very small in the beginning. The large discrepancy at 4:00 may be related to the difference in heat storage of wall during the daytime and wind velocity around the wall.

Analysis of diurnal cycle characteristic (daily average temperature and DTR)

The temperature variation during the whole day (24 hours) can be represented as a sinusoidal function, daily average temperature ($\overline{<\bar{T}_{wall}>}$) and daily temperature range (*DTR*) are always used to describe the diurnal cycle variations of urban thermal environment. We compare the diurnal cycle characteristics of $<\bar{T}_{wall}>$ of canopies with different aspect ratios (*H/W*=1, 2, 3) and thermal capacities (hollow and sand model). The wall temperature data measured by thermocouples from May 6th-June 10th, 2017 are selected here. The daily average temperature ($\overline{<\bar{T}_{wall}>}$) is calculated as the mean value of $<\bar{T}_{wall}>$ during the whole day. The *DTR of* $<\bar{T}_{wall}>$ is calculated as the difference between maximum temperature ($<\bar{T}_{wall}>_{max}$) and minimum temperature ($<\bar{T}_{wall}>_{min}$) during the whole day.

Fig. 9a shows the result of $\overline{<\bar{T}_{wall}>}$ for each day during the study period (each column represents data on the same day, some data for the sand model are lost and

cannot be shown here). For hollow models, $\overline{<\bar{T}_{wall}>}$ of the wider street (*H/W*=1) is always higher than the narrower street (*H/W*=2, 3), as wider street always receives more solar radiation during the daytime. However there is no significant difference in $\overline{<\bar{T}_{wall}>}$ between *H/W*=2 and 3. As the radiation processes in the street canyon include both shading and trapping effect, it seems that the radiation exchange process in the street canyon becomes more complicated when *H/W* is larger than 2. Further study will be needed to quantify the exact mechanisms. The above results are generally consistent with the findings of Wang et al. (2018). As shown in Fig. 9a-b, for models with same aspect ratio, $\overline{<\bar{T}_{wall}>}$ of the hollow model are higher than the sand model in sunny days (e.g. May 11th, 2017), however it is the opposite in cloudy days (e.g. May 13th, 2017) when the solar radiation flux is relatively weaker, though the difference is very small.

Then Fig. 9c presents the *DTR* of $<\bar{T}_{wall}>$ for each day during the study period (each column represents data on the same day, some data for the sand model are lost and cannot be shown here). For models with the same heat capacity, *DTR* of $<\bar{T}_{wall}>$ of the wider street (*H/W*=1) is always larger than the narrower streets (*H/W*=2, 3). The wider street (*H/W*=1) absorbs more solar radiation than narrower street (*H/W*=2, 3) during the daytime, thus the maximum temperature is much higher. At night, however, the wider street (*H/W*=1) loses more heat producing the relatively lower minimum temperature. For canopies with the same aspect ratio but different heat capacity, *DTR* of $<\bar{T}_{wall}>$ of hollow model is always higher than the sand model, highlights the impact of thermal storage on the diurnal temperatures, that the $<\bar{T}_{wall}>_{max}$ of

hollow model is larger while $< \bar{T}_{wall} >_{min}$ is smaller than the sand model.

To further analyze the detailed information of different aspect ratios and building heat capacity, we averaged the multi-day wall temperature characteristics over the period May 6th to June 10th 2017 (only data of 9 days are valid) which are listed in Table 5. For the hollow model, larger aspect ratio leads to lower maximum temperature (i.e. 36.4, 35.0, 34.5 ℃ for *H/W*=1, 2, 3, respectively). For the minimum temperature, the differences between various aspect ratios are very small (i.e. less than 0.4 ℃). Consequently, the daily temperature range (*DTR*) as *H/W*=1 (hollow model) is the largest (12.1 ℃), which is 1.2 and 2.1 ℃ larger than that of aspect ratios *H/W*=2, 3, respectively. Moreover, the sand model with larger thermal capacity experiences the lower maximum temperature but higher the minimum temperature than the hollow model. *DTR* of hollow model is 4.5, 4.6 and 3.8 ℃ larger than sand model with the aspect ratio of 1, 2, 3, respectively.

However, the differences in daily average temperature between different cases are much smaller, i.e. less than 0.6 ℃ for different aspect ratios and 0.2 ℃ for different thermal capacities. More significantly, for both hollow and sand models, wider streets (*H/W*=1) experience a little higher daily average temperature (0.3-0.6 ℃) than narrower ones (*H/W*=2, 3).

Analysis of heat storage flux calculated from thermocouple temperature

The increasing human-made structures of the city, such as buildings and roads, absorb heat during the daytime and release heat at night, producing more noticeable

heat storage effect than rural area. The magnitude of heat storage ΔQ_s affects the diurnal cycle temperature of a street or urban district. Offerle et al. (2005) proposed the element surface temperature method (ESTM) to estimate the total heat storage flux in cities through the surface temperature. The calculation formula is:

$$\Delta Q_s = \sum_i \frac{\Delta T_i}{\Delta t} s_i \Delta x_i \lambda_{pi} \quad (3)$$

where $\Delta T/\Delta t$ is the rate of temperature change over the period, s is the volumetric heat capacity, Δx is the element height, λ_p is the plan area fraction (fraction of the element plan area to the total street canyon plan area) and *i* represents the basic units in street canyon, including building roof, building wall, internal building expressed as iBLD (for hollow model, it is air; for sand model, it is sand), ground and external air (Fig. 10a). So $\Delta x \lambda_p$ represents the total element volume over the plan area, for each element *i*. The detailed thermo-physical properties of basic elements in the ideal street canyon for heat storage estimation are given in Table 6. The spatially-averaged temperature measured by thermocouples for each basic unit is used to calculate the temperature change rate of 10 minutes. ΔQ_s based on this temperature change rate is performed hourly average.

Fig. 10b shows the example of total heat storage flux ΔQ_s and its heat storage from different canopy components (roof, wall, iBLD, ground and external air) of hollow model (*H/W*=3) on May 17th, 2017. The value of ΔQ_s is positive during from 06:00 to 13:00 (building model absorbs heat), while the value of ΔQ_s is negative after 14:00 till early morning next day (building model releases heat). The heat storage in the hollow model mainly depends on the ground, building wall, and

building roof while the contributions of iBLD and external air are small.

Fig. 10c displays the example of total heat storage flux ΔQ_s and its heat storage from different urban components of sand model (*H/W*=3) on May 17th, 2017. The diurnal pattern of ΔQ_s of sand model is similar to hollow model. The value of ΔQ_s of sand model shows that the model absorbs heat from 06:00 to14:00, which is 1 hour more than the hollow model because of larger heat capacity. Moreover, compared with the hollow model, the heat storage of iBLD is obviously increased, which becomes the major part of heat storage in sand model due to its bigger heat capacity.

Fig. 10d shows the diurnal hourly ΔQ_s of hollow and sand model (*H/W*=1, 2, 3) over the period May 6th -June 10th, 2017 (data from 9 days with valid measurements and no rainfall). The differences in ΔQ_s between different aspect ratios are small while the difference is much bigger between different thermal capacities. The sand model absorbs and releases more heat than hollow model. The magnitude of ΔQ_s of sand model is 2.2 times (*H/W*=1), 2.8 times (*H/W*=2), 3.2 times (*H/W*=3) larger than hollow model on average. In the late afternoon, the hollow model starts to release heat earlier than the sand model. The sand model with larger heat capacity slows down the response to heat. The detailed information about the ratios of heat storage component of each city unit to the total heat storage flux in the heat absorption and release period are listed in Table 7.

During the heat absorption period (ΔQ_s>0), for the hollow model, the increment of the aspect ratio contributes to an increase of heat storage flux of wall, from 23.72% (*H/W*=1) to 39.11% (*H/W*=2) and 50.13% (*H/W*=3). The proportion of heat storage

flux of roof is smaller than the wall. The proportions of heat storage flux of roof are 7.00%, 13.48%, 19.94% for the canyons with aspect ratios of 1, 2, 3 respectively. For external air and iBLD in hollow model, the variations of both heat storage components are small, they contribute less than 1% to the total heat storage flux due to the smaller heat capacity of air. However, increase of the aspect ratio leads to a decrease of heat storage flux of ground from 68.48% to 46.44% and 28.83% in the street canyons with aspect ratio equal to 1, 2, 3. As material of most surfaces in the experiment are the same (roof, wall and ground), the differences in the contributions from various components between heat storage flux of surface and aspect ratio are due to the differences in total volume over the plan area ($\Delta x \lambda_p$) of each surface. $\Delta x \lambda_p$ of ground decreases as the aspect ratio increases, while $\Delta x \lambda_p$ of wall and roof increases with the aspect ratio.

The variations of heat storage proportion of the corresponding unit in sand model in terms of the change of aspect ratio are similar to the hollow model. However, the proportion of heat storage flux of iBLD is significantly increased. Consequently, the proportions of heat storage flux of other components are larger in the hollow model than those in sand model with the same aspect ratio. The heat storage flux of iBLD becomes the primary source of total heat storage flux of sand model. What's more, similar results can be observed during the heat release period (ΔQ_s<0).

3.7 Limitation and future work

Scaled outdoor measurement of urban models, which are the simplification of

realistic urban areas, have been proved to be a useful approach to study the physical processes of urban climate (Kanda, 2006). Our study presents outdoor scaled street canyon models that the key urban parameters, such as the aspect ratio and thermal storage can be flexibly controlled and modified, however in real city it is difficult. In contrast to full-scale street canyons, the scaled model used in the present study can attain the flow phenomena when wind-driven dynamic force dominates or both thermal buoyancy and wind-driven dynamic forces are significant and interact, but hardly get buoyancy-force-dominated urban airflow with sufficiently large *Re* at the same time. Nevertheless, based on the large amount of data from one month extensive measurements, the results show our scaled model is a good option to quantify the relative significance and impacts of urban parameters on urban climate. This paper first considers 2D street canyons (H/W=1, 2, 3) that are built by concrete building blocks (H=1.2 m), to investigate the influence of aspect ratio and thermal storage on urban thermal environment. The present study is focusing more on the diurnal cycle characteristics of air and surface temperature within the urban canopy.

Further investigations will be performed to examine the relative importance of factors within the complex energy-exchange processes, including heat storage of building and ground, fluxes of shortwave radiation, longwave radiation and sensible heat in 2D street canyon or 3D urban districts, which will make new contribution to the understandings of the spatial and temporal features of urban thermal environment and energy balance. In addition, our experiment can also provide high-quality parametric field data that can be used in the validation and to improve the accuracy of

numerical simulations and theoretical models. Moreover, further attention will also be paid to adopt more urban parameters, such as greenery, into our scaled outdoor experiment, to investigate the quantitative impacts of different urban parameters on urban micro-climate, and then provide meaningful guidance for sustainable urban climate design.

4. Conclusion

The street aspect ratio and thermal storage capacity are two essential urban parameters that largely determine urban micro-climate, such as the urban heat island and urban turbulence characteristics. However, the complex energy-exchange processes and the exact mechanisms of the impacts from both factors are still rarely investigated so far. In this study, we conducted a scaled outdoor field measurement to investigate the influence of street aspect ratios (H=1.2 m, H/W=1, 2, 3) and building heat storage (hollow and sand model) on urban thermal environment. The daily average temperature and daily temperature range (DTR) are adopted as key indexes of diurnal cycle characteristics. The conclusions are as following.

(1) The obvious diurnal-cycle characteristics of wall and air temperature are observed. The wall heats up in the morning, and reaches the highest temperature in the afternoon (around 15:00), then it cools down in the late afternoon till night due to longwave radiation and convective ventilation cooling. Furthermore, the weather condition and solar radiation play the significant role on daily cycle of wall temperature. A single peak of wall temperature occurs on sunny day, while the wall

temperature decreases in the cloudy days due to the reduction of solar radiation.

(2) The upper levels of the wall that receive more solar radiation experience higher temperature than the lower levels during the daytime. However, the upper levels tend to be cooled down faster due to the better ventilation and greater longwave radiation loss at night. Compared with wall temperature, the variation of air temperature at different heights of the central street canyon is small due to the significant turbulent mixing. The maximum surface-air temperature differences can reach up to 10-12 ℃ during our study period.

(3) The wall receiving more solar radiation with less shading area usually experiences higher temperature. During the daytime, wider street canyon (*H/W*=1) warms up faster and presents larger hot area proportion (the proportion of the wall temperature over 35 ℃ to the total wall temperature). However, at night, wider street canyon (*H/W*=1) cools down quicker and shows a larger cold area proportion (the proportion of the wall temperature below 28 ℃ to the total wall temperature) than narrower street canyons (*H/W*=2, 3). As a result, the daily average temperature and daily temperature range (*DTR*) of wider street canyon (*H/W*=1) are always higher than narrower street canyon (*H/W*=2, 3). According to ensemble mean of diurnal features of wall temperature, the differences in the daily average temperature between three aspect ratios are small (i.e. less than 0.6 ℃). But for *DTR*, as *H/W*=1 (i.e. hollow model) is 12.1 ℃, which is 1.2 and 2.1 ℃ larger than aspect ratio of *H/W*=2, 3, respectively. In addition, the impact of street aspect ratio on the average temperature and temperature range is more significant at lower level (*z*=0.3 m) than upper level

(z=1.1 m) during the daytime (the absorption of solar radiation at lower level is more sensitive to the change in aspect ratio than upper level), while such impact is small on both lower and upper level at night.

(4) The sand model with larger heat capacity exhibits the slower changing rate of the wall temperature. During the daytime, the hollow model (larger hot area proportion and smaller heat storage flux) warms up faster and stores less heat than the sand model (smaller hot area proportion and greater heat storage flux). However, at night, the sand model (smaller cold area proportion and higher heat storage flux) is warmer and releases more heat than hollow model. Therefore, *DTR* of hollow model are always greater than the sand model. From ensemble mean of diurnal characteristics of wall temperature, the differences in the daily average temperature with different thermal capacity are small (i.e. less than 0.2 ℃). *DTR* of hollow model is 4.5, 4.6 and 3.8 ℃ larger than sand model with the aspect ratio of 1, 2, 3, respectively.

Although further investigations are still required to reveal the influencing mechanisms of urban thermal environment and provide practical guidelines, this paper is one of the first attempts to develop a parametric scaled outdoor field measurement, to experimentally quantify how street aspect ratios, thermal storage and weather conditions influence daily cycle characteristics of urban air-wall temperatures. The effective methodologies are proposed for more urban morphologies and building thermal capacities with various meteorological conditions. By coupling with massive experimental data of radiation fluxes and turbulence characteristics, present results

can be adopted to provide validation and evaluation for theoretical models and numerical simulations.

Acknowledgements

This study was financially supported by National Key Research and Development Program of China [2016YFC0202206, 2016YFC0202205 and 2016YFC0202204], the National Science Fund for Distinguished Young Scholars (China, No. 41425020), the National Natural Science Foundation-Outstanding Youth Foundation (China, No. 41622502), STINT (Sweden, dnr CH2017-7271), the National Natural Science Foundation of China (No. 51811530017 and 41875015) as well as the State Key Program of National Natural Science Foundation (China, No. 91644215) and the Key projects of Guangdong Natural Science Foundation (China, No. 2018B030311068). The help from Mr Jianlin Yang, Dr Yifan Fan and Lei Peng is also gratefully acknowledged.

References

Aida M. Urban albedo as a function of the urban structure—A model experiment. Boundary-layer meteorology 1982; 23: 405-413.

Allegrini J, Dorer V, Carmeliet J. Wind tunnel measurements of buoyant flows in street canyons. Building and Environment 2013; 59: 315-326.

Allegrini, J, Dorer, V, Carmeliet, J. Buoyant flows in street canyons: Validation of CFD simulations with wind tunnel measurements. Building and Environment

2014; 72: 63-74.

Antoniou N, Montazeri H, Neophytou M, Blocken B. CFD simulation of urban microclimate: Validation using high-resolution field measurements. Science of the Total Environment 2019; 695: 133743.

Arnfield AJ. Two decades of urban climate research: a review of turbulence, exchanges of energy and water, and the urban heat island. International Journal of Climatology 2003; 23: 1-26.

Athamena K, Sini JF, Rosant JM, Guilhot J. Numerical coupling model to compute the microclimate parameters inside a street canyon. Solar Energy 2018a; 170: 470-485.

Athamena K, Sini JF, Rosant JM, Guilhot J. Numerical coupling model to compute the microclimate parameters inside a street canyon. Solar Energy 2018b; 174: 1237-1251.

Britter RE, Hanna SR. Flow and dispersion in urban areas. Annual Review of Fluid Mechanics 2003; 35: 469-496.

Chatterjee S, Khan A, Dinda A, Mithun S, Khatun R, Akbari H, Kusaka H, Mitra C, Bhatti SS, Doan QV, Wang YP. Simulating micro-scale thermal interactions in different building environments for mitigating urban heat islands. Science of the Total Environment 2019; 663: 610-631.

Chen L, Hang J, Sandberg M, Claesson L, Di Sabatino S, Wigo H. The impacts of building height variations and building packing densities on flow adjustment and city breathability in idealized urban models. Building and Environment 2017;

118: 344-361.

Cui PY, Li Z, Tao WQ. Wind-tunnel measurements for thermal effects on the air flow and pollutant dispersion through different scale urban areas. Building and Environment 2016; 97: 137-151.

Dallman A, Magnusson S, Britter R, Norford L, Entekhabi D, Fernando HJS. Conditions for thermal circulation in urban street canyons. Building and Environment 2014; 80: 184-191.

Eliasson I, Offerle B, Grimmond CSB, Lindqvist S. Wind fields and turbulence statistics in an urban street canyon. Atmospheric Environment 2006; 40: 1-16.

Fan YF, Li YG, Hang J, Wang K, Yang XY. Natural convection flows along a 16-storey high-rise building. Building and Environment 2016; 107: 215-225.

Fan, YF, Li YG, Yin S. Interaction of multiple urban heat island circulations under idealised settings. Building and Environment 2018a; 134:10-20.

Fan YF, Li YG, Yin S. Non-uniform ground-level wind patterns in a heat dome over a uniformly heated non-circular city. International Journal of Heat and Mass Transfer 2018b, 124:233-246.

Fernando HJS, Zajic D, Di Sabatino S, Dimitrova R, Hedquist B, Dallman A. Flow, turbulence, and pollutant dispersion in urban atmospheres. Physics of Fluids 2010; 22: 051301.

Fung WY, Lam KS, Hung WT, Pang SW, Lee YL. Impact of urban temperature on energy consumption of Hong Kong. Energy 2006; 31: 2623-2637.

Giannopoulou K, Santamouris M, Livada I, Georgakis C, Caouris Y. The impact of

canyon geometry on intra urban and urban: suburban night temperature differences under warm weather conditions. Pure and Applied Geophysics 2010; 167: 1433-1449.

Grimmond CSB, Roth M, Oke TR, Au YC, Best M, Betts R, Carmichael G, Cleugh H, Dabberdt W, Emmanuel R, Freitas E, Fortuniak K, Hanna S, Klein P, Kalkstein LS, Liu CH, Nickson A, Pearlmutter D, Sailor D, Voogt J. Climate and more sustainable cities: climate information for improved planning and management of cities (Producers/Capabilities Perspective). Procedia Environmental Sciences 2010; 1: 247-274.

Gromke C, Buccolieri R, Di Sabatino S, Ruck B. Dispersion study in a street canyon with tree planting by means of wind tunnel and numerical investigations – evaluation of CFD data with experimental data. Atmospheric Environment 2008; 42: 8640-8650.

Gu ZL, Zhang YW, Cheng Y, Lee SC. Effect of uneven building layout on airflow and pollutant dispersion in non-uniform street canyons. Building and Environment 2011; 46:2657-2665.

Hang J, Wang Q, Chen XY, Sandberg M, Zhu W, Buccolieri R, Di Sabatino S. City breathability in medium density urban-like geometries evaluated through the pollutant transport rate and the net escape velocity. Building and Environment 2015; 94:166-182.

Hang J, Luo ZW, Wang XM, He LJ, Wang BM, Zhu W. The influence of street layouts and viaduct settings on daily carbon monoxide exposure and intake

fraction in idealized urban canyons. Environmental Pollution 2017; 220: 72-86.

Harman IN, Best MJ, Belcher SE. Radiative exchange in an urban street canyon. Boundary-Layer Meteorology 2004; 110: 301-316.

Hass AL, Ellis KN. Using wearable sensors to assess how a heatwave affects individual heat exposure, perceptions, and adaption methods. International Journal of Biometeorology 2019; 63: 1585-1595.

Hong B, Lin BR. Numerical studies of the outdoor wind environment and thermal comfort at pedestrian level in housing blocks with different building layout patterns and trees arrangement. Renewable Energy 2015; 73: 18-27.

Johansson E. Influence of urban geometry on outdoor thermal comfort in a hot dry climate: A study in Fez, Morocco. Building and Environment 2006; 41: 1326-1338.

Kanda M, Kawai T, Nakagawa K. A simple theoretical radiation scheme for regular building arrays. Boundary-Layer Meteorology 2005; 114: 71-90.

Kanda M. Progress in the scale modeling of urban climate: Review. Theoretical and Applied Climatology 2006; 84: 23-33.

Kawai T, Kanda M. Urban energy balance obtained from the comprehensive outdoor scale model experiment. Part I: basic features of the surface energy balance. Journal of Applied Meteorology and Climatology 2010a; 49: 1341-1359.

Kawai T, Kanda M. Urban energy balance obtained from the comprehensive outdoor scale model experiment. Part II: comparisons with field data using an improved energy partition. Journal of Applied Meteorology and Climatology 2010b; 49:

1360-1376.

Kovar-Panskus A, Moulinneuf L, Savory E, Abdelqari A, Sini JF, Rosant JM, Robins A, Toy N. A wind tunnel investigation of the influence of solar-induced wall-heating on the flow regime within a simulated urban street canyon. Water, Air and Soil Pollution: Focus 2002; 2: 555-571.

Lai DY, Liu WY, Gan TT, Liu KX, Chen QY. A review of mitigating strategies to improve the thermal environment and thermal comfort in urban outdoor spaces. Science of the Total Environment 2019; 661: 337-353.

Li Q, Bou-Zeid E, Anderson W, Grimmond S, Hultmark M. Quality and reliability of LES of convective scalar transfer at high Reynolds numbers. International Journal of Heat and Mass Transfer 2016; 102: 959-970.

Liang WH, Huang JX, Jones P, Wang Q, Hang J. A zonal model for assessing street canyon air temperature of high-density cities. Building and Environment 2018; 132: 160-169.

Lin M, Hang J, Li YG, Luo ZW, Sandberg M. Quantitative ventilation assessments of idealized urban canopy layers with various urban layouts and the same building packing density. Building and Environment 2014; 79: 152-167.

Lin L, Hang J, Wang XX, Wang XM, Fan SJ, Fan Q, Liu YH. Integrated effects of street layouts and wall heating on vehicular pollutant dispersion and their reentry toward downstream canyons. Aerosol and Air Quality Research 2016; 16: 3142-3163.

Louka P, Vachon G, Sini JF, Mestayer PG, Rosant JM. Thermal effects on the airflow

in a street canyon–Nantes' 99 experimental results and model simulations. Water, Air, and Soil Pollution: Focus 2002; 2: 351-364.

Lu J, Arya SP, Snyder WH, Lawson RE Jr. A laboratory study of the urban heat island in a calm and stably stratified environment. Part I: Temperature field. Journal of Applied Meteorology 1997; 36: 1377-1391.

Mackey CW, Lee X, Smith RB. Remotely sensing the cooling effects of city scale efforts to reduce urban heat island. Building and Environment 2012; 49: 348-358.

Manoli G, Fatichi S, Schlapfer M, Yu KL, Crowther TW, Meili N, Burlando P, Katul GG, Bou-Zeid E. Magnitude of urban heat islands largely explained by climate and population. Nature 2019; 573: 55-60.

Meroney R, Ohba R, Leitl B, Kondo H, Grawe D, Tominaga Y. Review of CFD guidelines for dispersion modeling. Fluids 2016; 1: 14.

Mora C, Dousset B, Caldwell IR, Powell FE, Geronimo RC, Bielecki CR, Counsell CW, Dietrich BS, Johnston ET, Louis LV, Lucas MP, McKenzie MM, Shea AG, Tseng H, Giambelluca T, Leon LR, Hawkins E, Trauernicht C. Global risk of deadly heat. Nature Climate Change 2017; 7: 501-506.

Nakamura Y, Oke TR. Wind, temperature and stability conditions in an east-west oriented urban canyon. Atmospheric Environment 1988; 22: 2691-2700.

Niachou K, Livada I, Santamouris M. Experimental study of temperature and airflow distribution inside an urban street canyon during hot summer weather conditions—Part I: Air and surface temperatures. Building and Environment

2008; 43: 1383-1392.

Offerle B, Grimmond CSB, Fortuniak K. Heat storage and anthropogenic heat flux in relation to the energy balance of a central European city centre. International Journal of Climatology 2005; 25: 1405-1419.

Offerle B, Eliasson I, Grimmond CSB, Holmer B. Surface heating in relation to air temperature, wind and turbulence in an urban street canyon. Boundary-Layer Meteorology 2007; 122: 273-292.

Oke TR. Canyon geometry and the nocturnal urban heat island: comparison of scale model and field observations. Journal of climatology 1981; 1: 237-254.

Oke TR. Street design and urban canopy layer climate. Energy and Buildings 1988; 11: 103-113.

Oke TR, Johnson GT, Steyn DG, Watson ID. Simulation of surface urban heat islands under ‘ideal’conditions at night Part 2: Diagnosis of causation. Boundary-Layer Meteorology 1991; 56: 339-358.

Oke TR, Mills G, Christen A, Voogt JA. Urban climates: Cambridge University Press, 2017.

Park M, Hagishima A, Tanimoto J, Narita K. Effect of urban vegetation on outdoor thermal environment: Field measurement at a scale model site. Building and Environment 2012; 56: 38-46.

Pearlmutter D, Berliner P, Shaviv E. Evaluation of urban surface energy fluxes using an open-air scale model. Journal of Applied Meteorology 2005; 44: 532-545.

Pearlmutter D, Berliner P, Shaviv E. Physical modeling of pedestrian energy exchange

within the urban canopy. Building and Environment 2006; 41: 783-795.

Pearlmutter D, Berliner P, Shaviv E. Integrated modeling of pedestrian energy exchange and thermal comfort in urban street canyons. Building and Environment 2007a; 42: 2396-2409.

Pearlmutter D, Berliner P, Shaviv E. Urban climatology in arid regions: current research in the Negev desert. International Journal of Climatology 2007b; 27: 1875-1885.

Peng SS, Piao SL, Ciais P, Friedlingstein P, Ottle C, Breon FM, Nan HJ, Zhou LM, Myneni RB. Surface urban heat island across 419 global big cities. Environmental Science & Technology 2012; 46: 696-703.

Richards K, Schatzmann M, Leitl B. Wind tunnel experiments modelling the thermal effects within the vicinity of a single block building with leeward wall heating. Journal of wind engineering and industrial aerodynamics 2006; 94: 621-636.

Salata F, Golasi L, Petitti D, Vollaro EDL, Coppi M, Vollaro ADL. Relating microclimate, human thermal comfort and health during heat waves: An analysis of heat island mitigation strategies through a case study in an urban outdoor environment. Sustainable Cities and Society 2017; 30: 79-96.

Santamouris M, Papanikolaou N, Koronakis I, Livada I, Asimakopoulos D. Thermal and air flow characteristics in a deep pedestrian canyon under hot weather conditions. Atmospheric Environment 1999; 33: 4503-4521.

Santamouris M. Cooling the cities – A review of reflective and green roof mitigation technologies to fight heat island and improve comfort in urban environments.

Solar Energy 2014; 103: 682-703.

Scungio M, Stabile L, Rizza V, Pacitto A, Russi A, Buonanno G. Lung cancer risk assessment due to traffic-generated particles exposure in urban street canyons: A numerical modelling approach. Science of the Total Environment 2018; 631-632: 1109-1116.

Silva HR, Bhardwaj R, Phelan PE, Golden JS, Grossman-Clarke S. Development of a zero-dimensional mesoscale thermal model for urban climate. Journal of Applied Meteorology and Climatology 2009; 48: 657-668.

Snyder WH. Similarity criteria for the application of fluid models to the study of air pollution meteorology. Boundary-Layer Meteorology 1972; 3: 113-134.

Song JY, Wang ZH. Interfacing the urban land–atmosphere system through coupled urban canopy and atmospheric models. Boundary-Layer Meteorology 2015; 154: 427-448.

Stewart ID, Oke TR. Local climate zones for urban temperature studies. Bulletin of the American Meteorological Society 2012; 93: 1879-1900.

Syafii NI, Ichinose M, Kumakura E, Jusuf SK, Chigusa K, Wong NH. Thermal environment assessment around bodies of water in urban canyons: A scale model study. Sustainable Cities Society 2017; 34: 79-89.

Toparlar Y, Blocken B, Vos P, van Heijst GJF, Janssen WD, van Hooff T, Montazeri H, Timmermans HJP. CFD simulation and validation of urban microclimate: A case study for Bergpolder Zuid, Rotterdam. Building and Environment 2015; 83: 79-90.

Uehara K, Murakami S, Oikawa S, Wakamatsu S. Wind tunnel experiments on how thermal stratification affects flow in and above urban street canyons. Atmospheric Environment 2000; 34: 1553-1562.

Wang K, Li YG, Li YH, Lin BR. Stone forest as a small-scale field model for the study of urban climate. International Journal of Climatology 2018; 38: 3723-3731.

Wang Q, Li YG, Hang J, Peng L. The diurnal cycle of urban thermal environment in scale-model street canyons by outdoor field measurement. Procedia Engineering 2017; 198: 743-757.

Xie XM, Huang Z, Wang JS, Xie Z. The impact of solar radiation and street layout on pollutant dispersion in street canyon. Building and Environment 2005; 40: 201-212.

Yam J, Li YG, Zheng ZH. Nonlinear coupling between thermal mass and natural ventilation in buildings. International Journal of Heat Mass Transfer 2003; 46: 1251-1264.

Yan H, Wu F, Dong L. Influence of a large urban park on the local urban thermal environment. Science of the Total Environment 2018; 622: 882-891.

Yang JC, Wang ZH, Kaloush KE. Environmental impacts of reflective materials: Is high albedo a ‘silver bullet’ for mitigating urban heat island? Renewable and Sustainable Energy Reviews 2015; 47: 830-843.

Yang LN, Li YG. City ventilation of Hong Kong at no-wind conditions. Atmospheric Environment 2009; 43: 3111-3121.

Yang XY, Li YG. The impact of building density and building height heterogeneity on average urban albedo and street surface temperature. Building and Environment 2015; 90: 146-156.

Yang XY, Li YG, Luo ZW, Chan PW. The urban cool island phenomenon in a high-rise high-density city and its mechanisms. International Journal of Climatology 2017; 37: 890-904.

Yee E, Biltoft CA. Concentration fluctuation measurements in a plume dispersing through a regular array of obstacles. Boundary-Layer Meteorology 2004; 111: 363-415.

Yuan C, Shan RQ, Zhang YY, Li XX, Yin TG, Hang J, Norford L. Multilayer urban canopy modelling and mapping for traffic pollutant dispersion at high density urban areas. Science of the Total Environment 2019; 647: 255-267.

Zhang K, Chen GW, Wang XM, Liu SH, Mak CM, Fan YF, Hang J. Numerical evaluations of urban design technique to reduce vehicular personal intake fraction in deep street canyons. Science of the Total Environment 2019; 653: 968-994.

Zhang YW, Gu ZL, Yu CW. Review on numerical simulation of airflow and pollutant dispersion in urban street canyons under natural background wind condition. Aerosol and Air Quality Research 2018; 18: 780-789.

Zhao L, Lee X, Smith RB, Oleson K. Strong contributions of local background climate to urban heat islands. Nature 2014; 511: 216-219.

Declaration of interests

☒ The authors declare that they have no known competing financial interests or personal relationships that could have appeared to influence the work reported in this paper.

☐The authors declare the following financial interests/personal relationships which may be considered as potential competing interests:

Guanwen Chen, Dongyang Wang, Qun Wang, Yuguo Li, Xuemei Wang, Jian Hang, Peng Gao, Cuiyun Ou, Kai Wang

CRediT author statement:

Guanwen Chen: Methodology, Software, Formal analysis, Writing - Original Draft, Visualization. **Dongyang Wang:** Methodology, Investigation. **Qun Wang:** Methodology, Formal analysis. **Yuguo Li:** Conceptualization, Resources. **Xuemei Wang:** Conceptualization, Resources. **Jian Hang:** Conceptualization, Formal analysis, Writing - Review & Editing, Supervision, Funding acquisition. **Peng Gao:** Conceptualization, Writing - Review & Editing. **Cuiyun Ou:** Conceptualization, Writing - Review & Editing. **Kai Wang:** Conceptualization, Investigation, Formal analysis, Writing - Review & Editing.

Fig. 1 (a) The experiment site of scaled outdoor field measurement and the direction of coordinate axis (positive *X*: south, positive *Y*: west, positive *Z*: vertical upward); Schematic illustration of: (b) the plan of street canyons (hollow & sand model) with aspect ratios *H/W*=1, 2, 3 and measurement positions in *X*-*Y* plane (top view); (c) the definitions of street canyon surfaces (roof, north wall, south wall and ground) in *X*-*Z* plane (side view).

Fig. 2 Schematic setup of the experimental instruments: (a) sonic anemometers, (b) thermocouples and ibuttons, (c) infrared camera

Fig. 3 Example figures showing diurnal cycle temperature in canyon measured on June 26th, 2017: (a) 24-hour infrared images of hollow model (south wall, *H/W*=1), (b) $\bar{T}_{wall}$ (hollow model, south wall, *H/W*=1) at different heights measured by thermocouples, (c) $\bar{T}_{air}$ (hollow model, *H/W*=1) at various heights along street centreline measured by ibuttons, (d) The difference of $<T_{wall}>$ (hollow model, north wall, *H/W*=3) between thermocouples and infrared camera, (e) $<\overline{T}>$ at wall, ground and roof, $<\overline{T}>$ of air within canyon (hollow model, *H/W*=1) measured by thermocouples, background air temperature $\bar{T}_b$ at z=2H and downward shortwave radiation measured by weather station during three consecutive days (May 18th - 20th, 2017)

Fig. 4 Example figures comparing wall temperature in canyon with different orientation (north & south wall, hollow model, *H/W* = 1), infrared images measured on June 26th, 2017: (a) during the daytime, (b) during the night; Diurnal variation of wall temperature (hollow model, *H/W*=1) measured by thermocouples including single point temperature $\bar{T}_{wall}$ and spatially-averaged temperature $<\bar{T}_{wall}>$, and downward shortwave radiation measured by weather station: (c) on May 28th, 2017, sunny day, (d) on June 9th, 2017, cloudy day

Fig. 5 Example figures comparing wall temperature in canyon with various aspect ratios (hollow model, *H/W* = 1, 2, 3): (a) Infrared images of south wall on June 26th, 2017, (b) $<\bar{T}_{wall}>$ at 8 points (north & south wall) measured by thermocouples on May 11th, 2017

Fig. 6 Example figures comparing wall temperature in canyon with different thermal capacity (hollow & sand model), infrared images of south wall measured on June 26th, 2017: (a) *H/W* = 1, (b) *H/W* = 2, (c) *H/W* = 3; $<\overline{T}_{wall}>$ at 8 points (north & south wall, *H/W*=1) measured by thermocouples and downward shortwave radiation measured by weather station: (d) on May 11th, 2017, (e) on June 9th, 2017

Fig. 7 Boxplots of wall temperature of the lower level (*z*=0.3 m) and upper level (*z*=1.1 m) on both north and south facades of hollow model with different aspect ratios (*H/W*=1, 2, 3), note: 7 days data selected from May 11th-June 9th, 2017: (a) during the daytime, 07:00-20:00, (b) during the night, 20:00-07:00

Fig. 8 Example figures showing hot area proportion (T_{wall} > 35 ℃) and cold area proportion (T_{wall} < 28 ℃) calculated from infrared data measured on June 26th, 2017: (a) diurnal variation (sand model, *H/W*=1, south wall), (b) different aspect ratio (*H/W*=1, 2, 3), south wall of the sand model, (c) different heat capacity (hollow and sand model), south wall with the aspect ratio 3, (d) different orientation (north and south wall), hollow model with the aspect ratio 1

Fig. 9 Diurnal cycle characteristics of $<\bar{T}_{wall}>$ with different aspect ratios (*H/W*=1, 2, 3) and thermal capacity (hollow and sand model) measured by thermocouples during the day, over the period of May 6th-June 10th, 2017: (a) $\overline{<\bar{T}_{wall}>}$, (b) Downward shortwave radiation measured by weather station: May 11th, 13th, 2017, (c) *DTR* of $<\bar{T}_{wall}>$, note: some data for sand model are lost and cannot be shown here.

Fig. 10 (a) Schematic illustration of basic units in street canyon, including roof, wall, internal building, ground and external air; Example figures showing total heat storage flux ΔQ_s and its heat storage components of street model (*H/W*=3) on May 17th, 2017: (b) hollow model, (c) sand model; (d) Diurnal hourly ΔQ_s of hollow and sand model (*H/W*=1, 2, 3) over the period May 6th-June 10th , 2017 (only data of 9 days are valid).

Table 1. Instruments for measurement

Measured parameter	Instrument	Horizontal position	Vertical position	Sampling rate	Quantity
Wind velocity within and above canyon	Sonic anemometer (Gill WindMaster)	Refer to Fig. 1b	Refer to Fig. 2a	20 Hz	22
Canyon air temperature	Ibutton (DS1922L)		Refer to Fig. 2b	10 min	30
Canyon surface and air temperature	Thermocouple (K-type, Φ0.255 mm)		Refer to Fig. 2b	1 min	246
Canyon wall temperature	Infrared camera (R500)		Refer to Fig. 2c	1 h	2
Background air temperature, wind speed, solar radiation and rainfall	Weather station (RainWise PortLog)		Height: 2.4 m (above the ground)	10 min	2

Table 2. Typical Reynolds number and bulk Richardson number in scaled urban airflow with characteristic reference values ($\Delta T = T_w - T_{ref}$=10 K, T_{ref}=300 K, H=1.2 m) during the experimental period

Aspect ratio (H/W)	Background reference velocity (U_{ref})	Reynolds number ($Re = U_{ref}H/\nu$)	bulk Richardson number ($Ri_b = \frac{gH\Delta T / T_{ref}}{U_{ref}^2}$)
1, 2, 3	0.1 m/s	8219	39.2
	0.5 m/s	41096	1.57
	2 m/s	164384	0.1

Table 3. Physical properties of street canyon materials (hollow model: concrete, sand model: concrete and sand)

Material	Density, ρ (g/cm^3)	Conductivity, λ (W/mK)	Diffusivity, D (mm^2/s)	Volumetric heat capacity, s (MJ/m^3K)	Emissivity, ε
Concrete	2.42	2.073	1.386	1.496	0.87
Sand	0.79	0.36	0.49	0.733	-

Table 4. Summary of the statistical performance of wall temperature measurement differences (mean absolute error MAE and root mean squared error RMSE) between

the infrared camera and thermocouple

Statistics	MAE (℃)	RMSE (℃)
Hollow model (*H/W*=3, north wall)	0.70	0.87

Table 5. Summary of the multi-day averaged wall temperature characteristics of different aspect ratios and building heat capacity over the period May 6th-June 10th, 2017 (only data of 9 days are valid)

Model type	Aspect ratio	T_{max}	T_{min}	DTR	$\bar{T}_{day}$
Hollow	*H/W* = 1	36.4	24.3	12.1	29.0
	H/W = 2	35.0	24.1	10.9	28.4
	H/W = 3	34.5	24.5	10.0	28.5
Sand	*H/W* = 1	33.4	25.7	7.6	28.8
	H/W = 2	32.2	25.8	6.3	28.5
	H/W = 3	31.9	25.7	6.2	28.3

Table 6. Properties of basic elements in the ideal model (hollow and sand model) for heat storage estimation

Element	Aspect ratio	Material	Volumetric heat capacity, s (MJK$^{-1}m^{-3}$)	Element height, Δx (m)	Plan area fraction, λ_p
Roof	*H/W*=1				0.294
	H/W=2	Concrete	1.496	0.015	0.455
	H/W=3				0.556
Wall	*H/W*=1				0.018
	H/W=2	Concrete	1.496	1.200	0.027
	H/W=3				0.033
Internal building	*H/W*=1	Air (for hollow model), Sand (for sand model)	1.211×10^{-3} (for air), 0.733 (for sand)	1.200	0.276
(iBLD)	*H/W*=2				0.427
	H/W=3				0.522
Ground	*H/W*=1	Concrete	1.496	0.100	0.706
	H/W=2				0.545

	H/W=3				0.444
External air	*H/W*=1				0.706
	H/W=2	Air	1.211×10^{-3}	1.200	0.545
	H/W=3				0.444

Table 7. Summary of the ratio (%) of heat storage component of each city unit to the total heat storage flux during the heat absorption ($\Delta Q_s > 0$) and release ($\Delta Q_s < 0$) period

Heat storage flux		ΔQ_s > 0					ΔQ_s < 0				
Model type	Aspect ratio	Wall	Roof	External air	Internal building	Ground	Wall	Roof	External air	Internal building	Ground
Hollow	*H/W* = 1	23.72	7.00	0.52	0.28	68.48	23.58	7.07	0.50	0.28	68.57
	H/W = 2	39.11	13.48	0.49	0.48	46.44	39.13	13.89	0.48	0.48	46.02
	H/W = 3	50.13	19.94	0.42	0.68	28.83	49.78	20.50	0.41	0.68	28.63
Sand	*H/W* = 1	10.90	5.30	0.34	37.02	46.44	11.25	5.71	0.34	33.67	49.03
	H/W = 2	14.28	8.90	0.24	52.49	24.09	14.84	9.75	0.25	49.42	25.74
	H/W = 3	16.07	9.83	0.17	57.52	16.41	16.65	10.68	0.17	54.94	17.56

Scaled outdoor measurements of urban climate(SOMUCH) in 2D street canyon are tested.

Impact of aspect ratio(H/W=1,2,3; H=1.2m)/thermal storage on T profiles is studied.

Wider street is warmer in daytime and cools down quicker at night than narrower one.

Sand models with more thermal mass get less daily temperature range(DTR) than hollow models.

Upper walls receive more radiation in daytime but cool down quicker than lower walls.

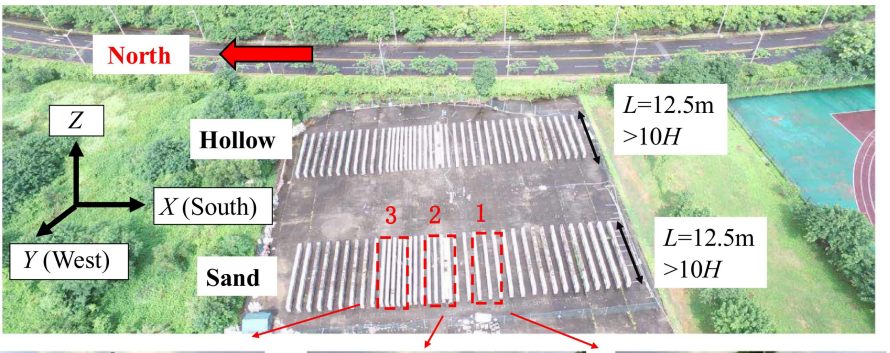

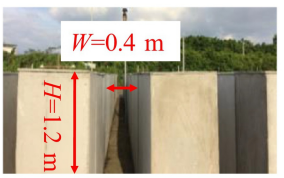

Aspect Ratio H/W=3

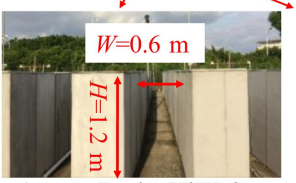

Aspect Ratio H/W=2

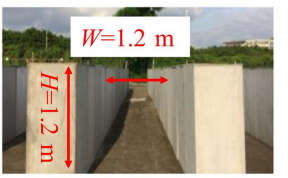

Aspect Ratio H/W=1

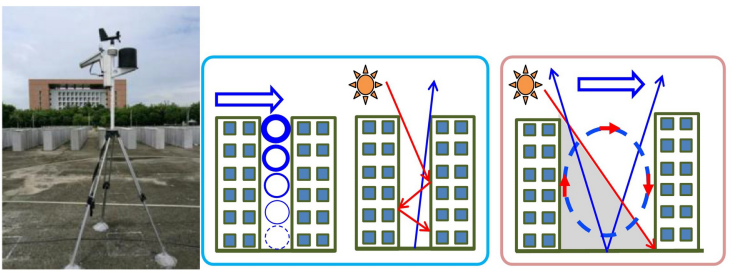

(a)

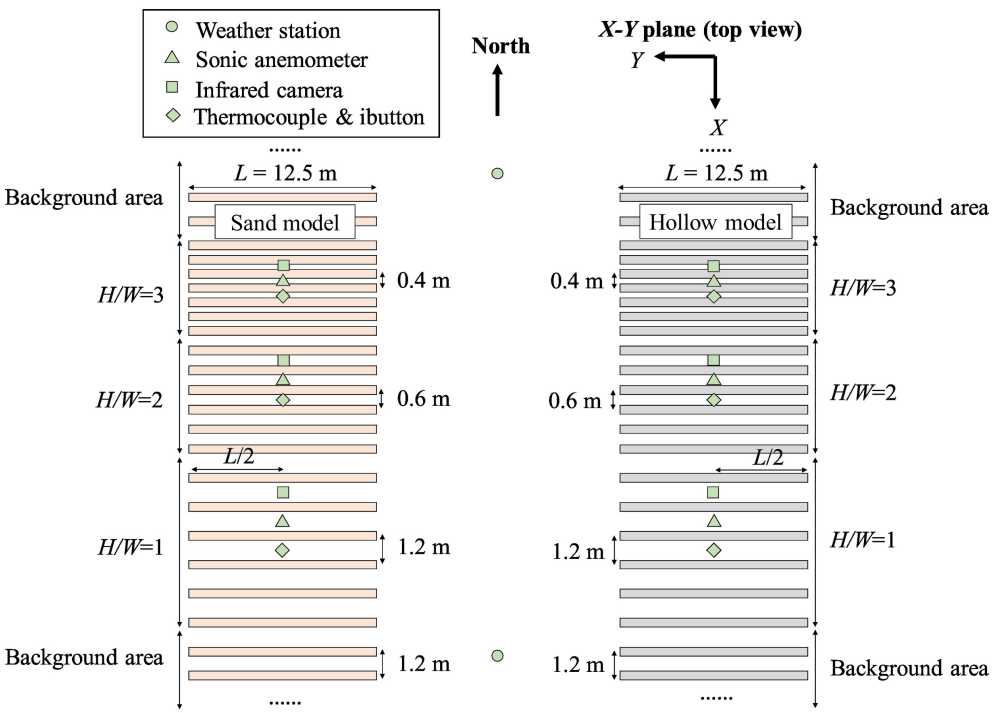

(b)

Figure 1ab

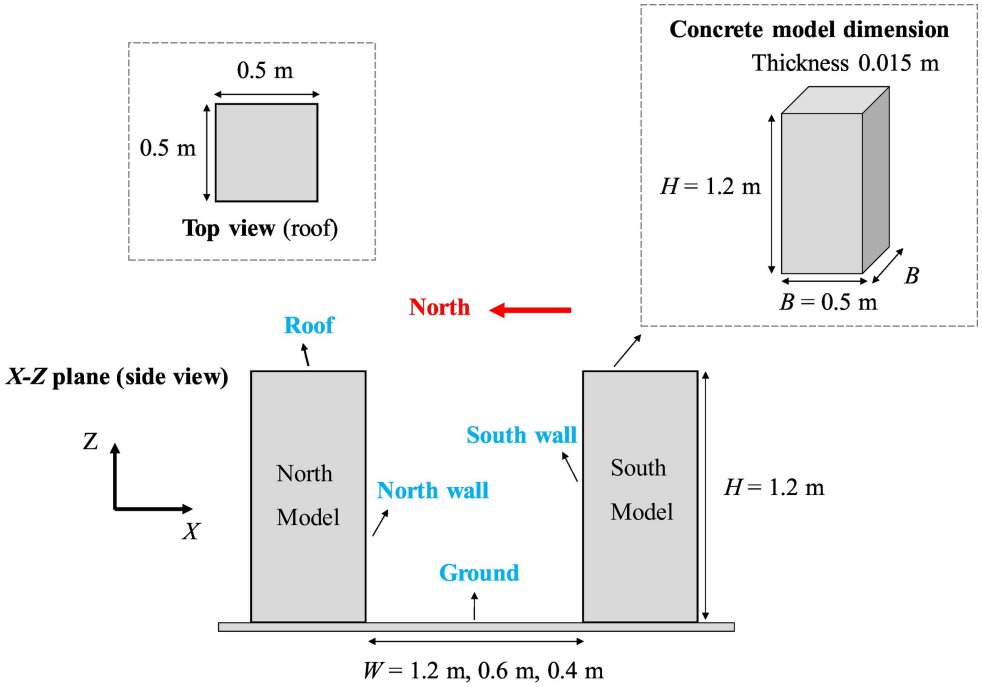
0.5 m
0.5 m
Top view (roof)
Concrete model dimension
Thickness 0.015 m
H = 1.2 m
B
B = 0.5 m
North
Roof
X-Z plane (side view)
Z
X
North Model
North wall
South wall
South Model
H = 1.2 m
Ground
W = 1.2 m, 0.6 m, 0.4 m

(c)

Figure 1c

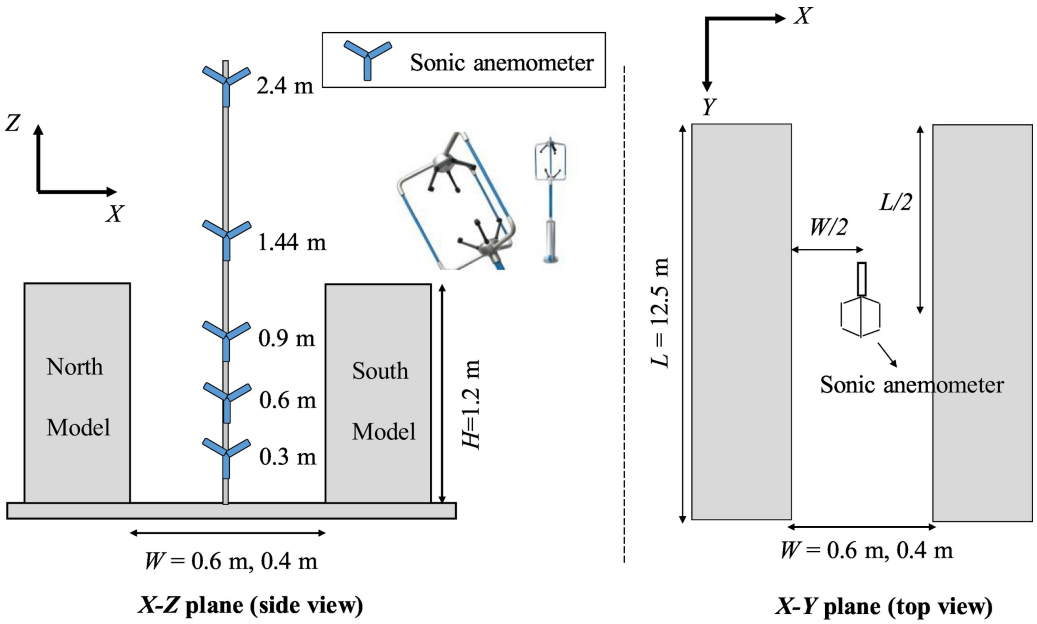

(a)

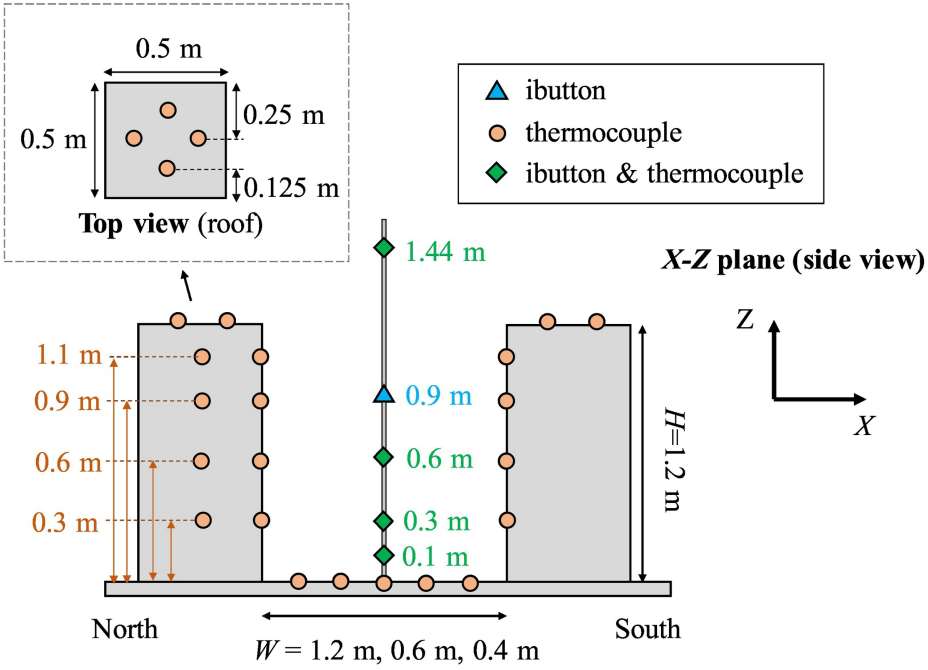

(b)

Figure 2ab

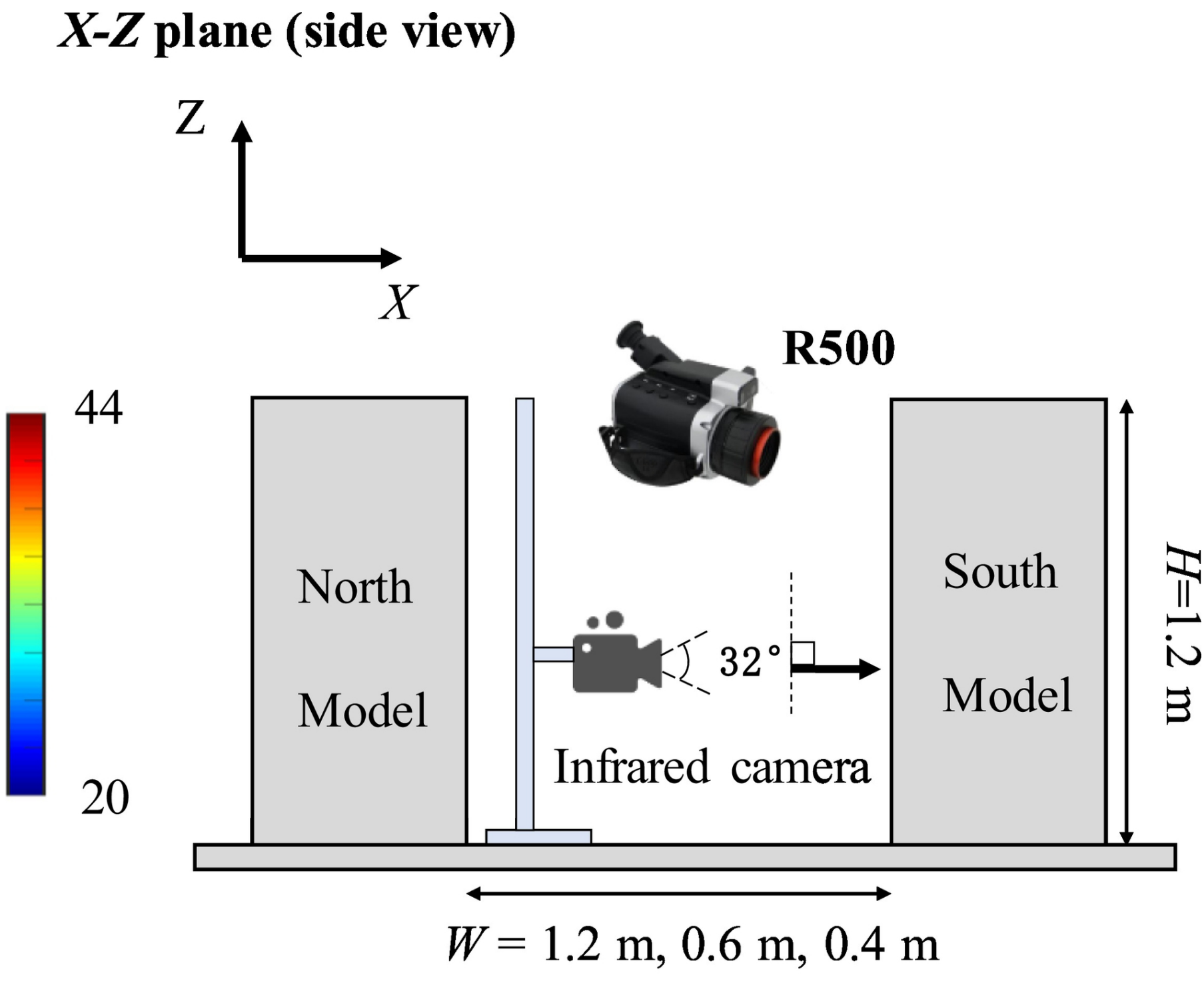
X-Z plane (side view)
Z
X
R500
44
20
North
Model
South
Model
H=1.2 m
32°
Infrared camera
W = 1.2 m, 0.6 m, 0.4 m

(c)

Figure 2c

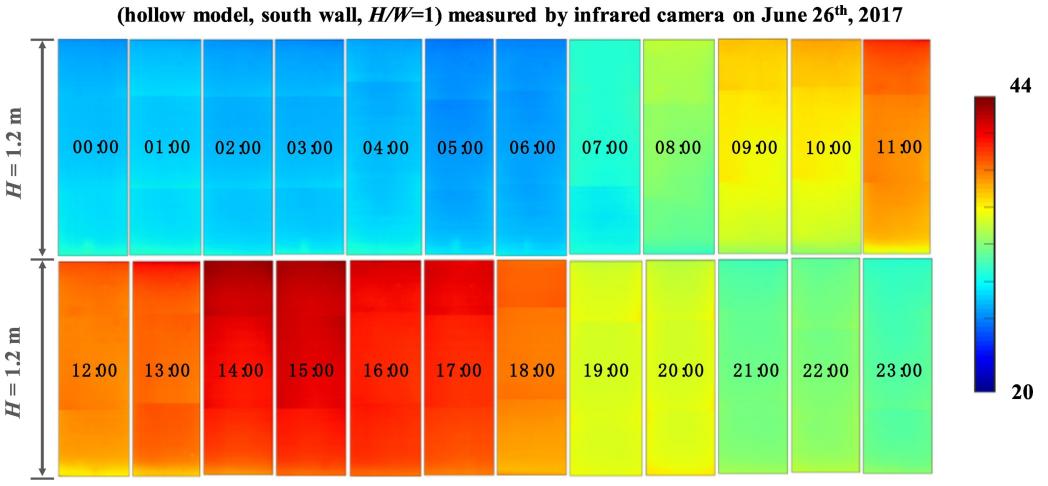

(a)

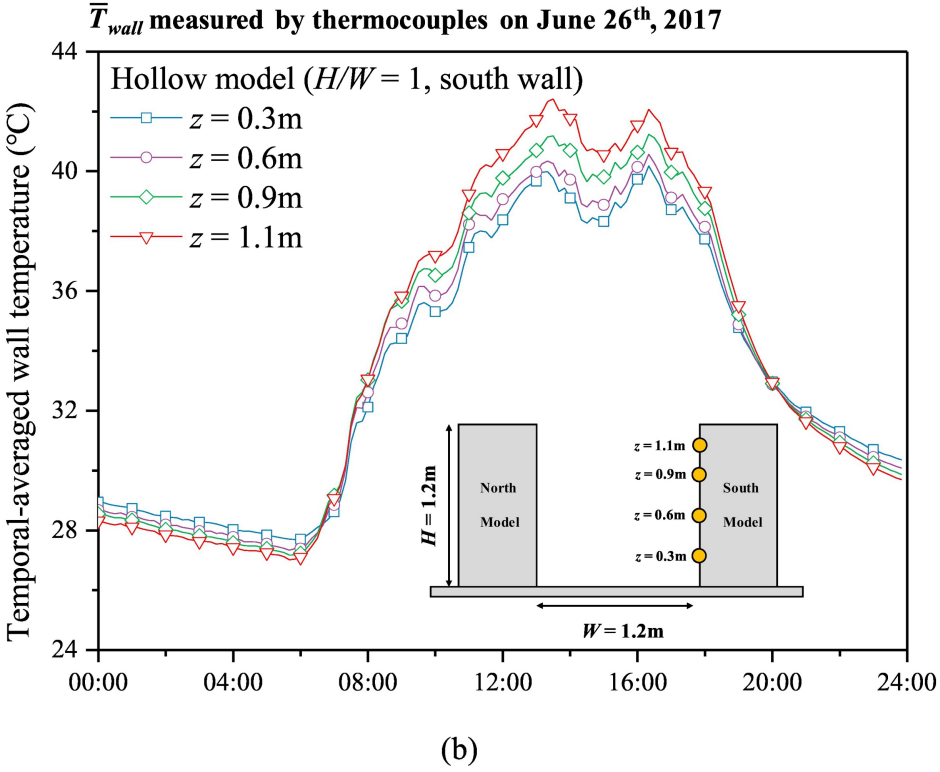

(b)

Figure 3ab

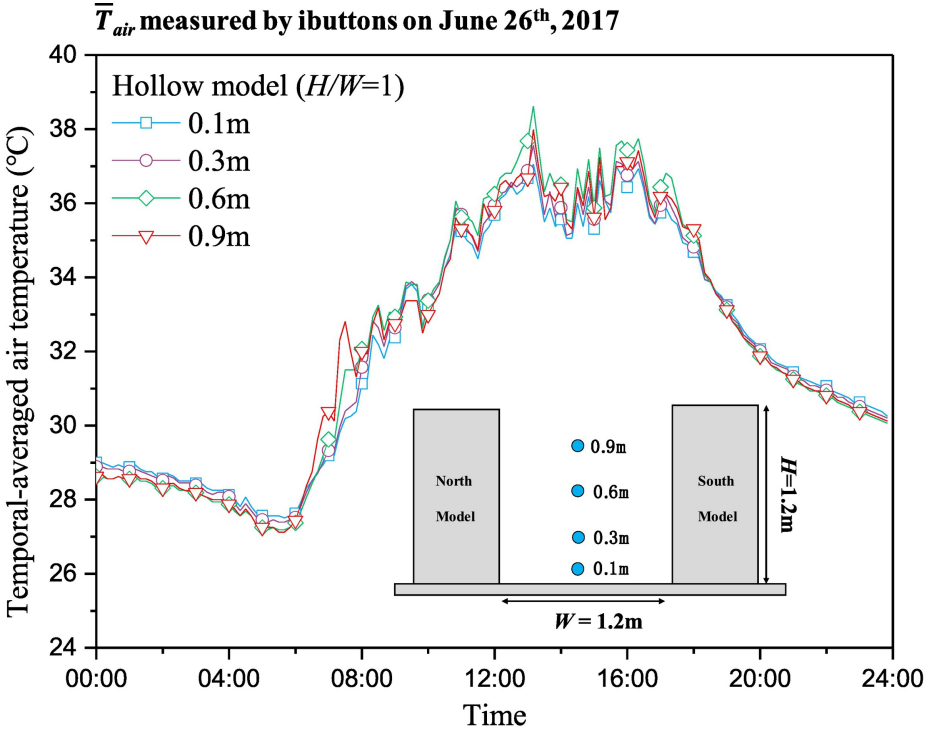

(c)

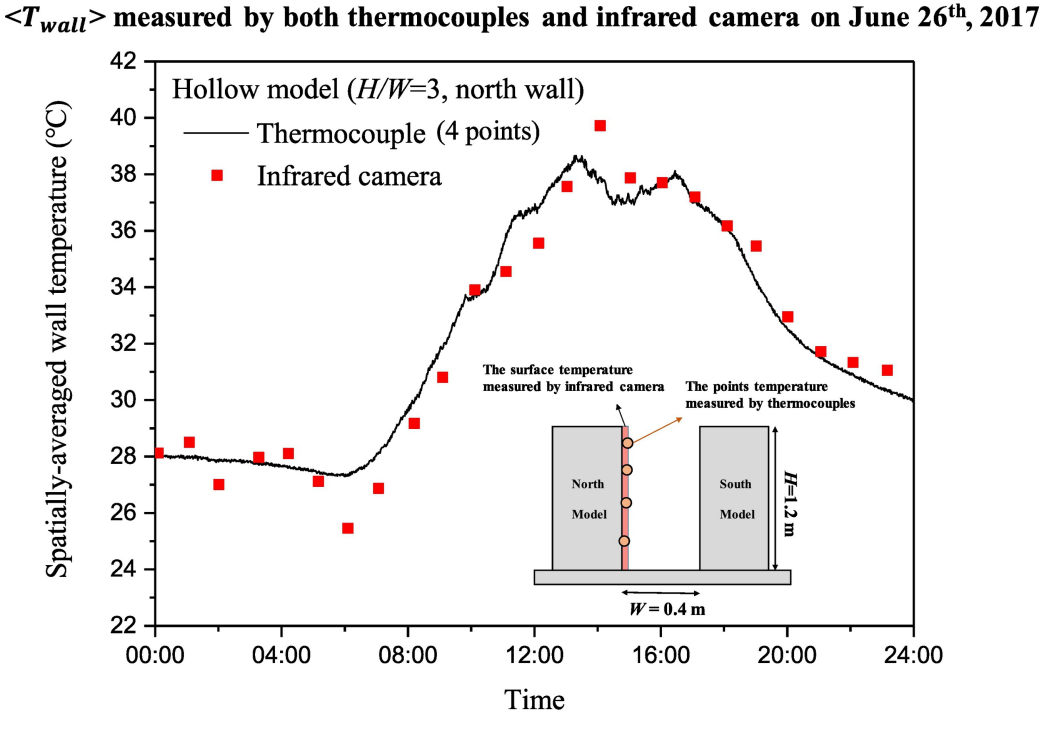

(d)

Figure 3cd

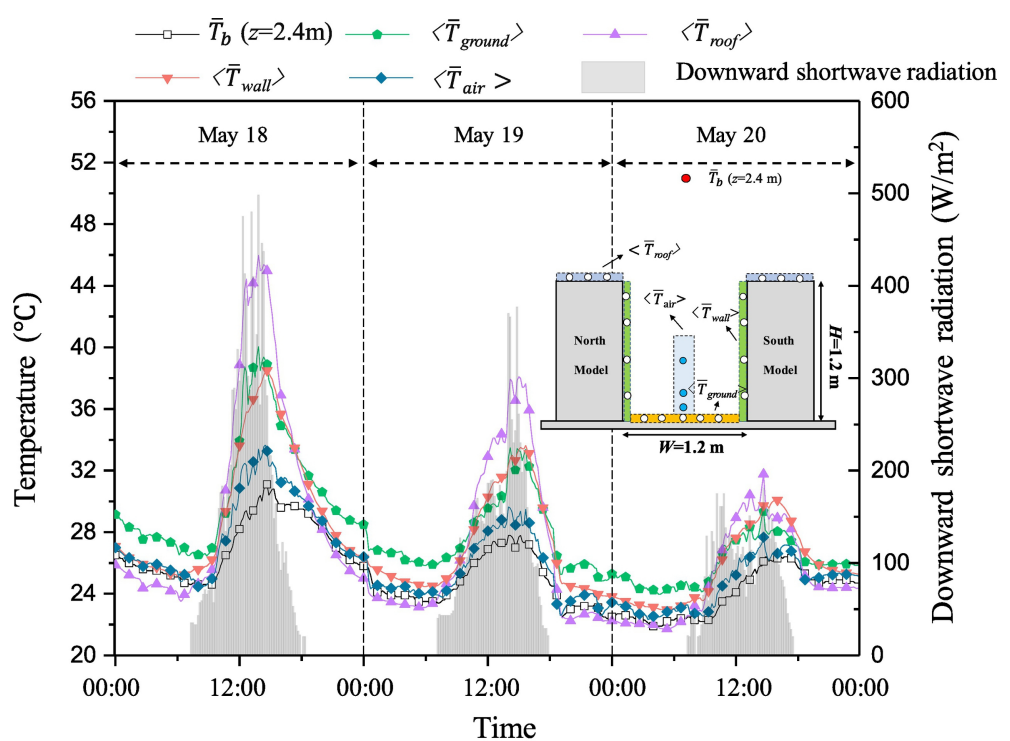
$\bar{T}_b$ (z=2.4m)
$\langle \bar{T}_{ground} \rangle$
$\langle \bar{T}_{roof} \rangle$
$\langle \bar{T}_{wall} \rangle$
$\langle \bar{T}_{air} \rangle$
Downward shortwave radiation
May 18
May 19
May 20
Temperature (°C)
Downward shortwave radiation (W/m²)
Time
00:00
12:00
$\bar{T}_b$ (z=2.4 m)
North Model
South Model
H=1.7 m
W=1.2 m

(e)

Figure 3e

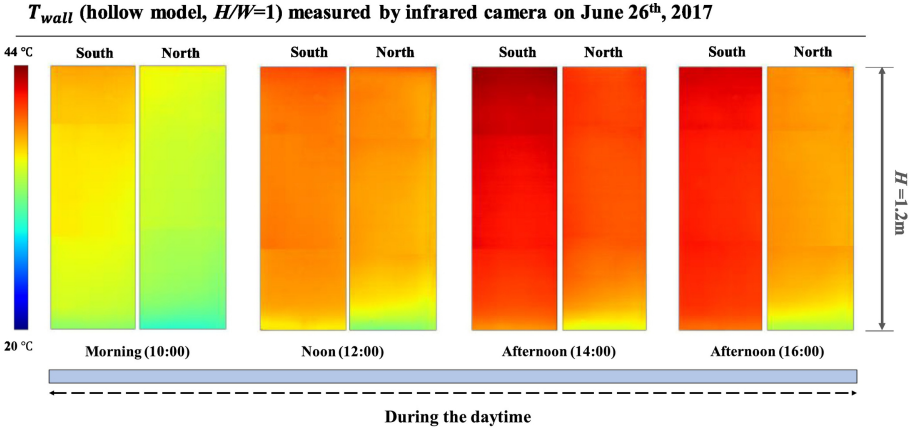

(a)

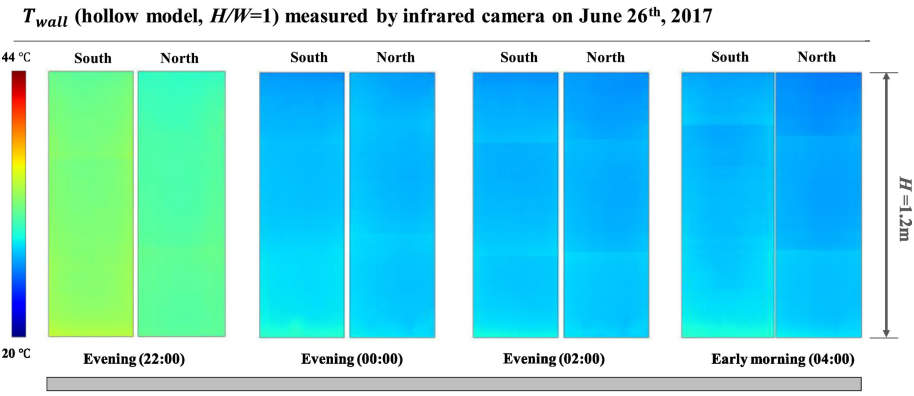

(b)

Figure 4ab

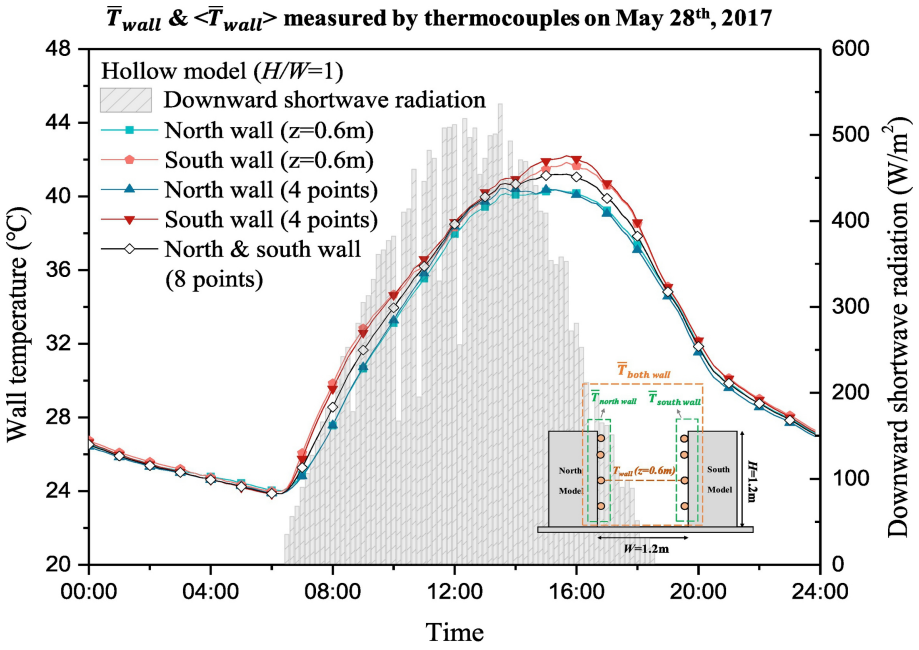

(c)

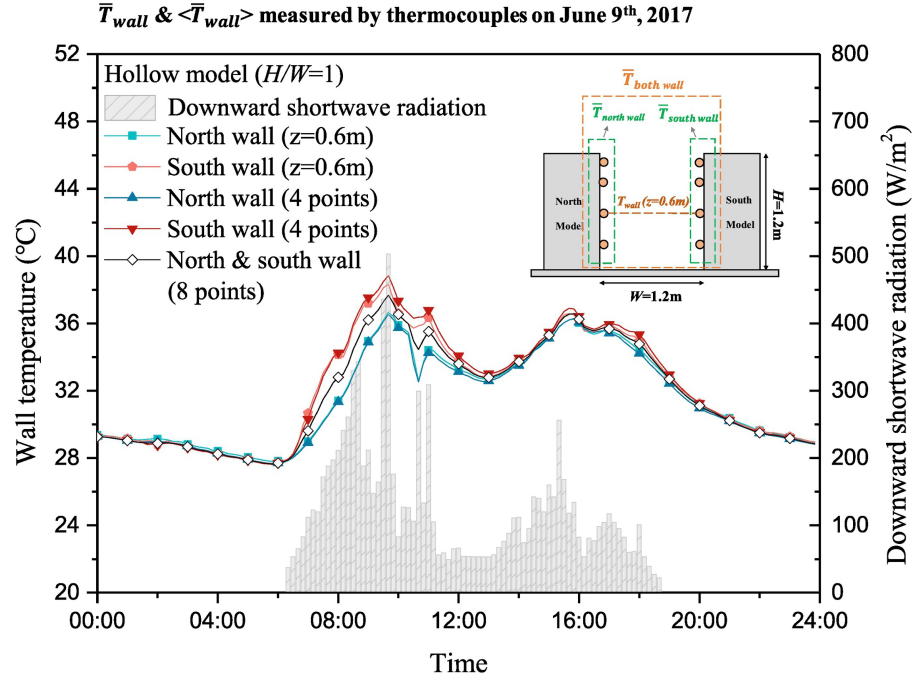

(d)

Figure 4cd

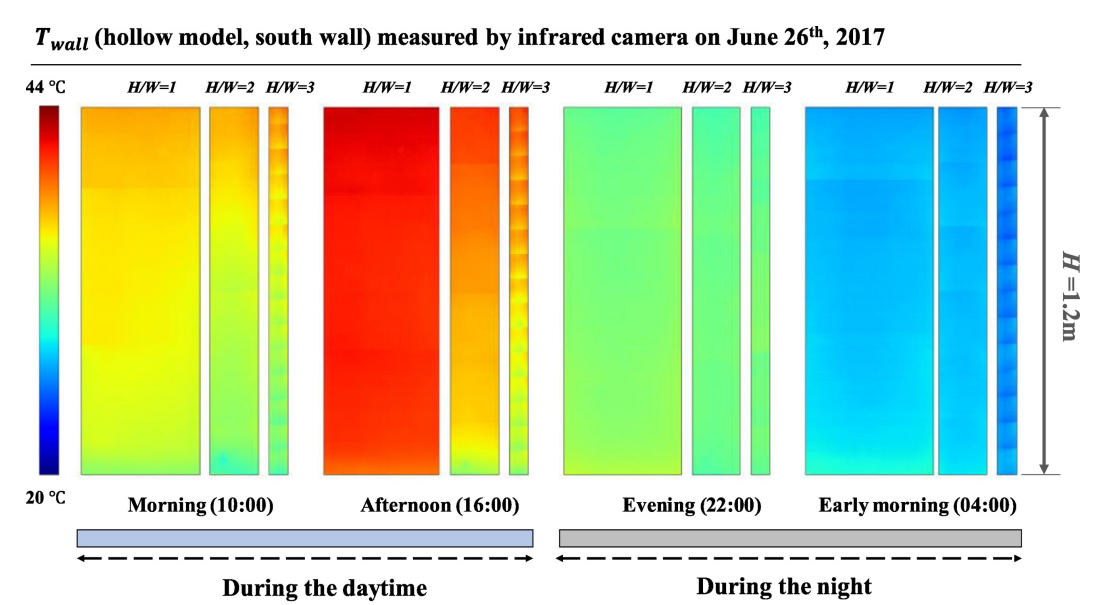

(a)

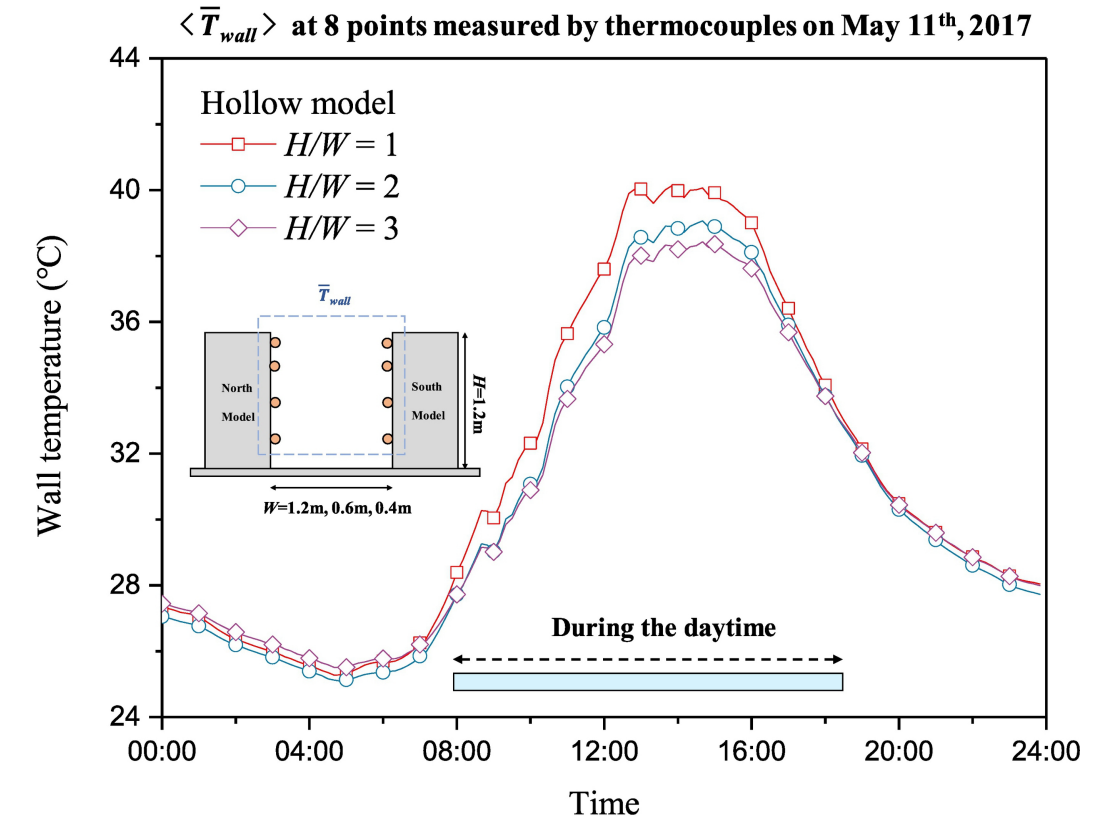

(b)

Figure 5ab

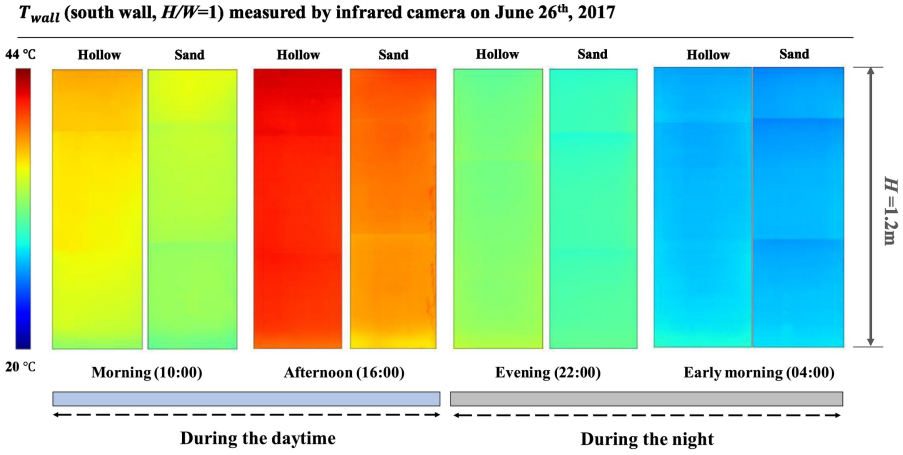

(a)

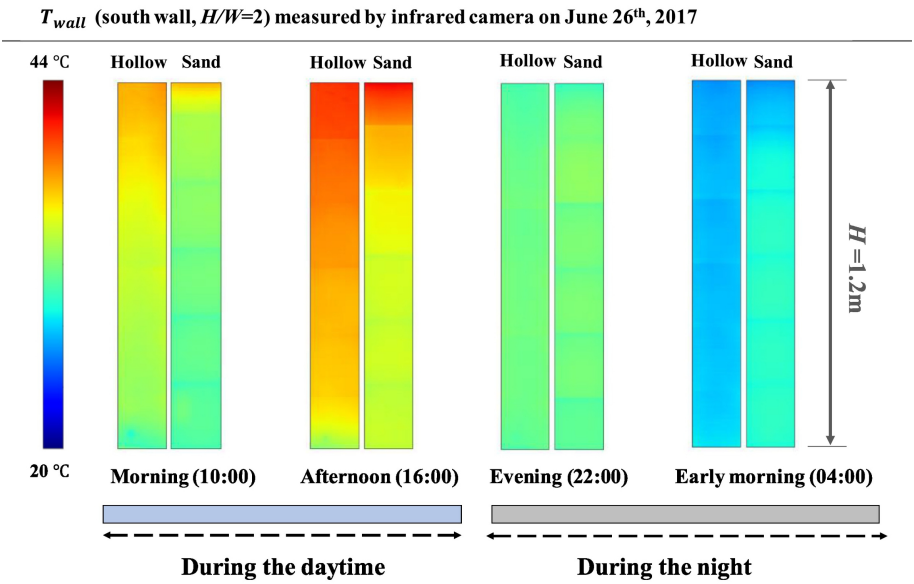

(b)

Figure 6ab

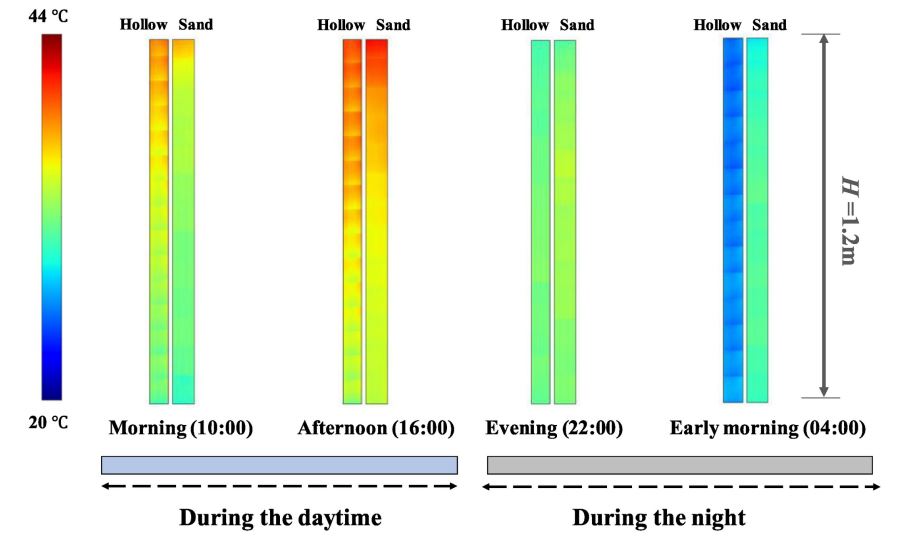

(c)

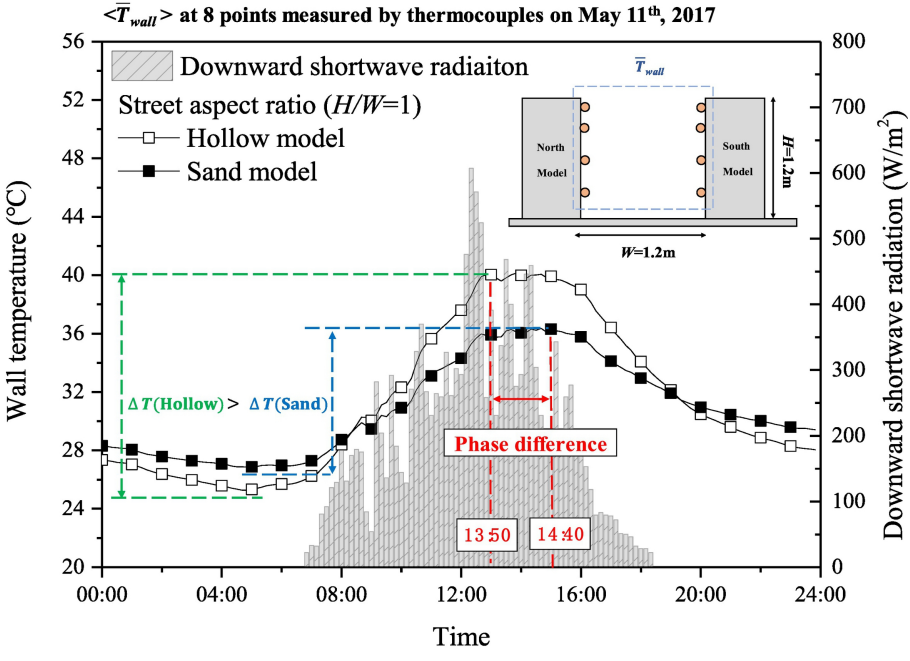

(d)

Figure 6cd

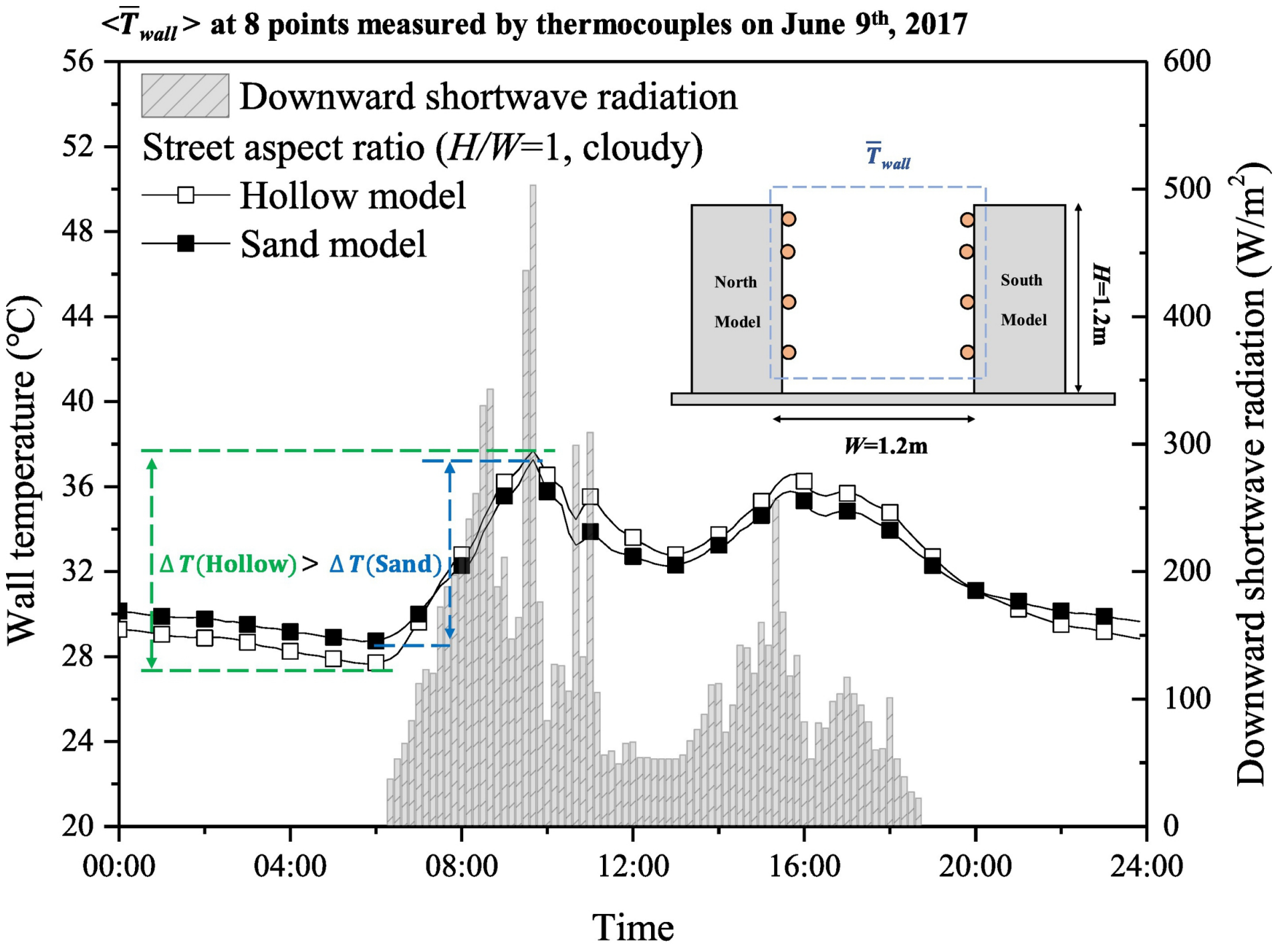
<$\overline{T}_{wall}$> at 8 points measured by thermocouples on June 9th, 2017
Downward shortwave radiation
Street aspect ratio (H/W=1, cloudy)
Hollow model
Sand model
$\overline{T}_{wall}$
North Model
South Model
H=1.2m
W=1.2m
ΔT(Hollow) > ΔT(Sand)
Wall temperature (°C)
Downward shortwave radiation (W/m²)
Time
00:00
04:00
08:00
12:00
16:00
20:00
24:00
20
24
28
32
36
40
44
48
52
56
0
100
200
300
400
500
600

(e)

Figure 6e

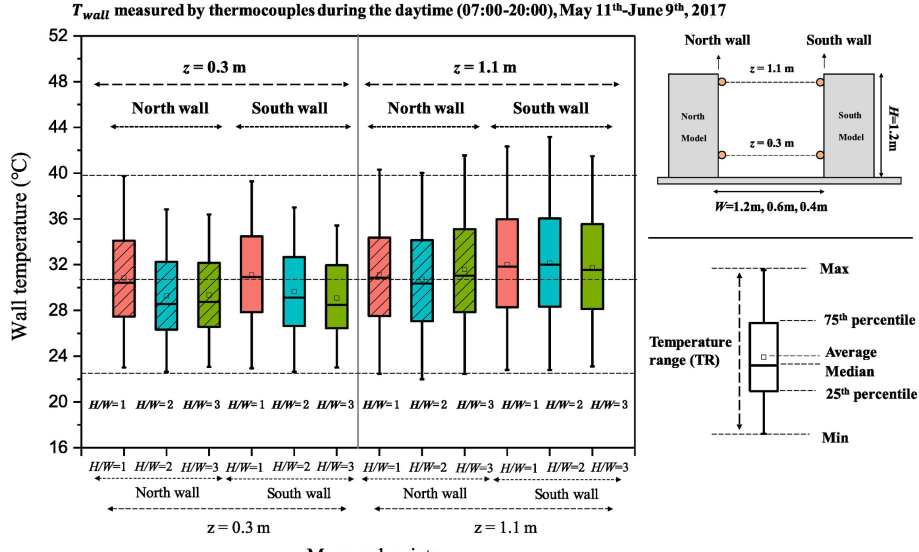

(a)

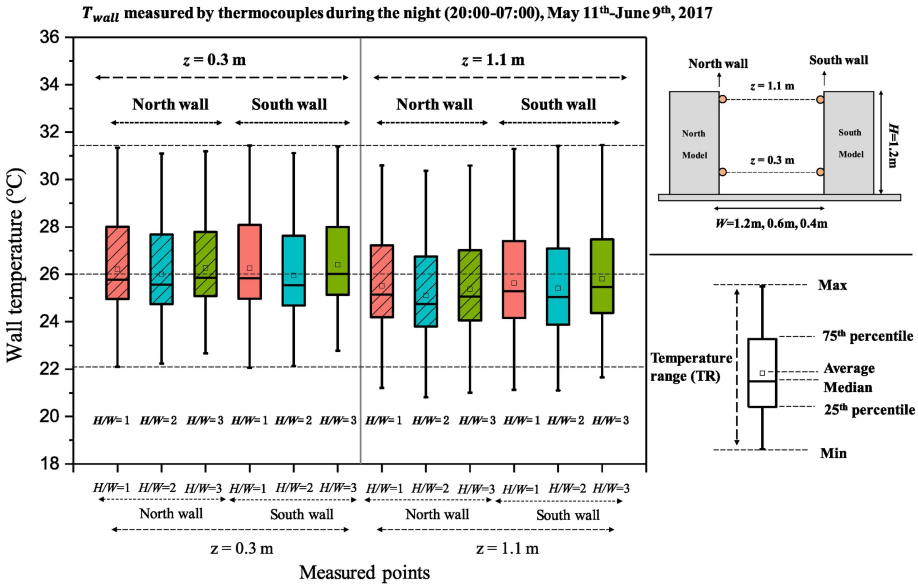

(b)

Figure 7ab

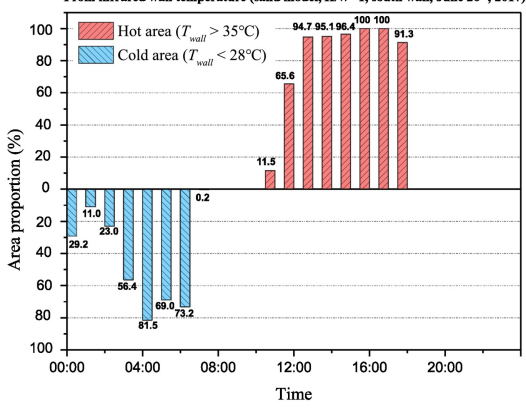

(a)

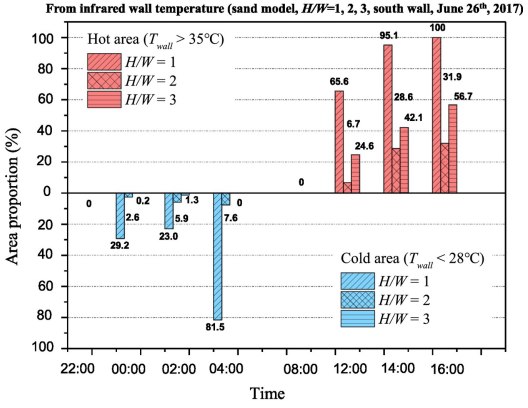

(b)

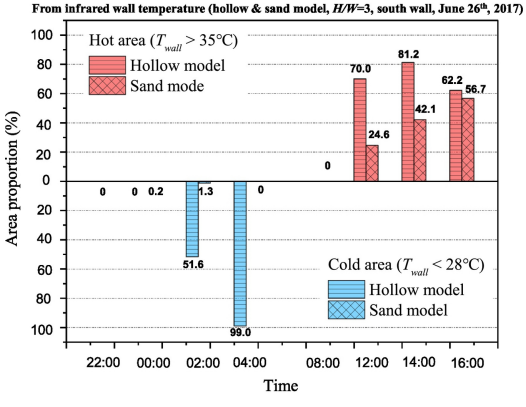

(c)

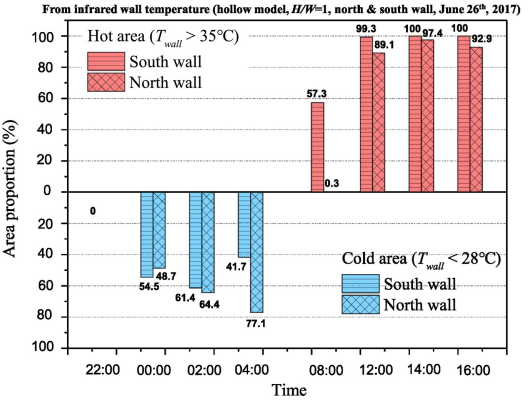

(d)

Figure 8

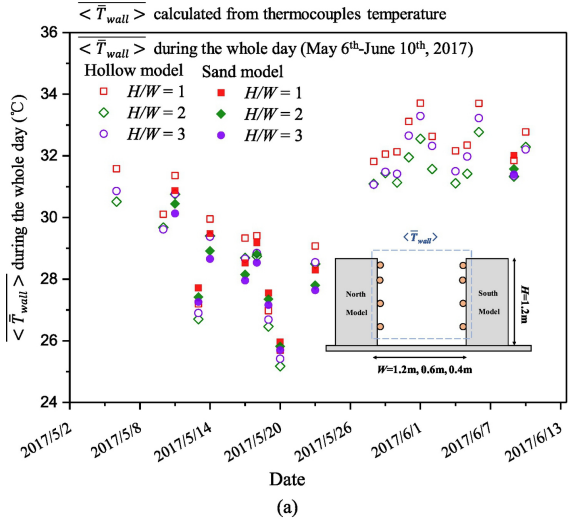
$\overline{<T_{wall}>}$ calculated from thermocouples temperature
$\overline{<T_{wall}>}$ during the whole day (May 6th-June 10th, 2017)
Hollow model
Sand model
H/W = 1
H/W = 2
H/W = 3
$\overline{<T_{wall}>}$ during the whole day (℃)
Date
North Model
South Model
H=1.2m
W=1.2m, 0.6m, 0.4m

(a)

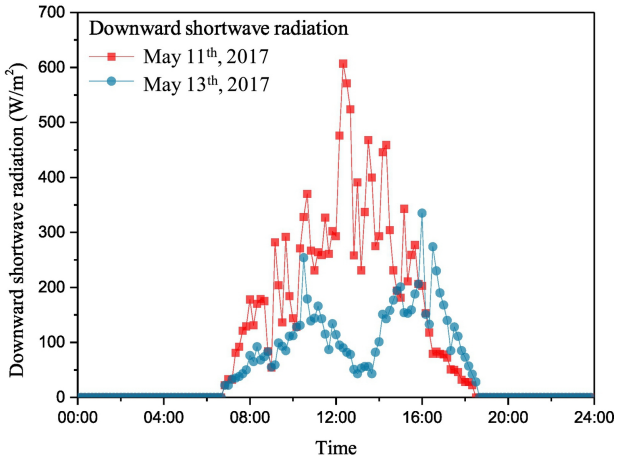
Downward shortwave radiation
May 11th, 2017
May 13th, 2017
Downward shortwave radiation (W/m²)
Time

(b)

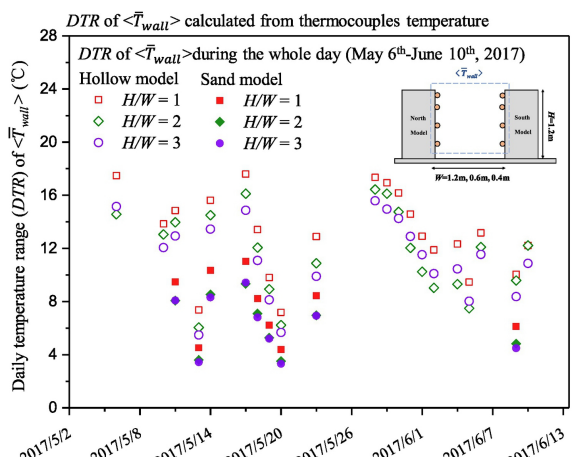
DTR of $<\overline{T}_{wall}>$ calculated from thermocouples temperature
DTR of $<\overline{T}_{wall}>$during the whole day (May 6th-June 10th, 2017)
Hollow model
Sand model
H/W = 1
H/W = 2
H/W = 3
Daily temperature range (DTR) of $<\overline{T}_{wall}>$ (℃)
Date
North Model
South Model
H=1.2m
W=1.2m, 0.6m, 0.4m

(c)

Figure 9

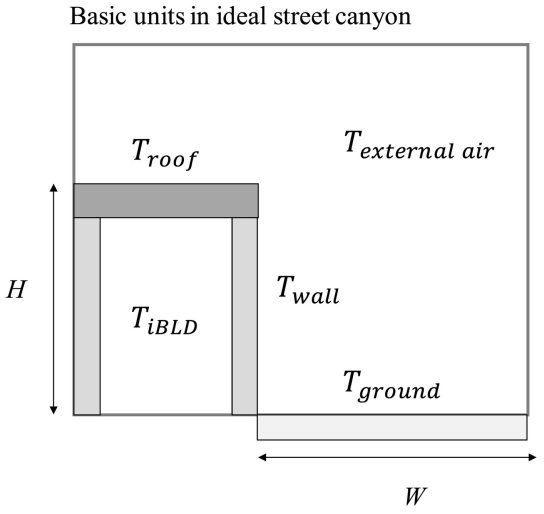

(a)

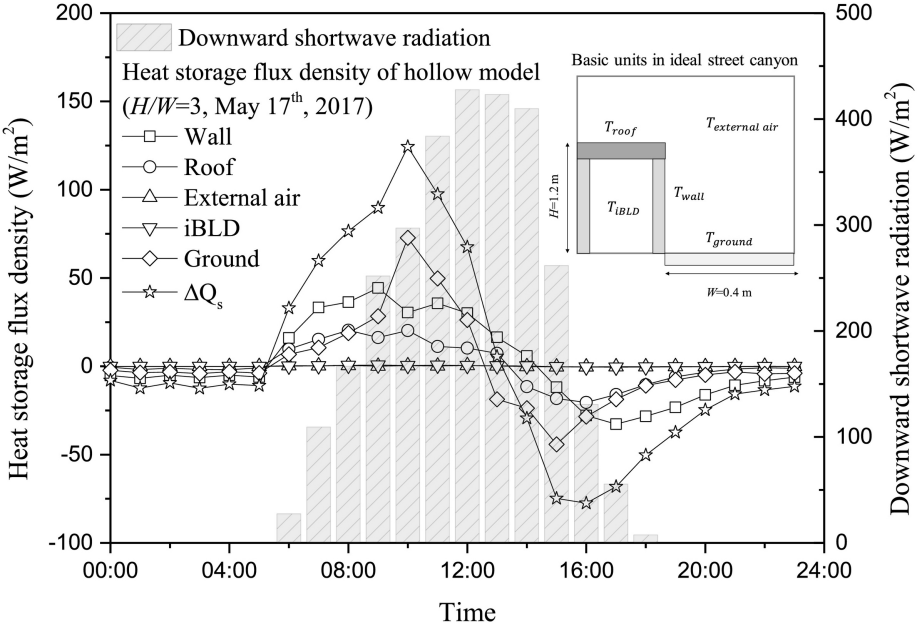

(b)

Figure 10ab

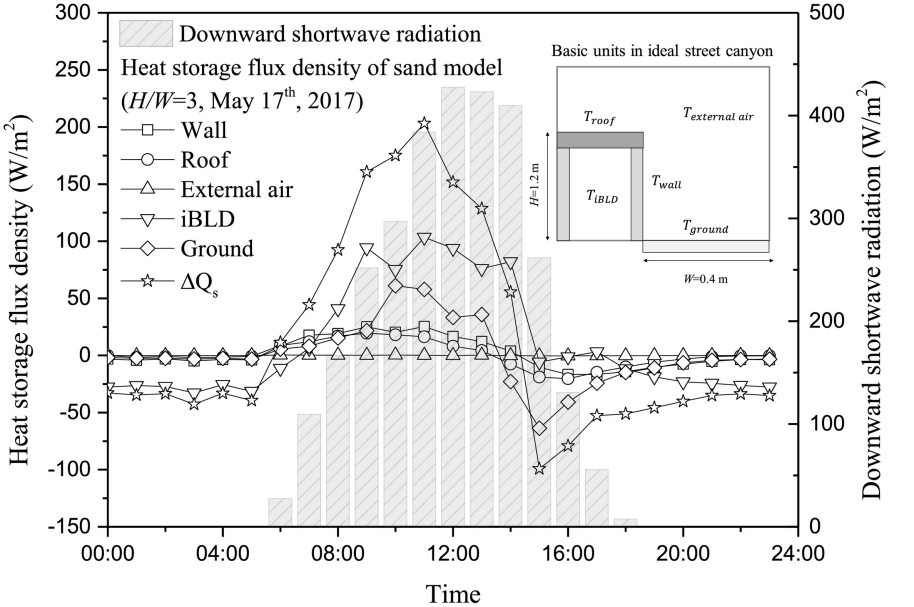

(c)

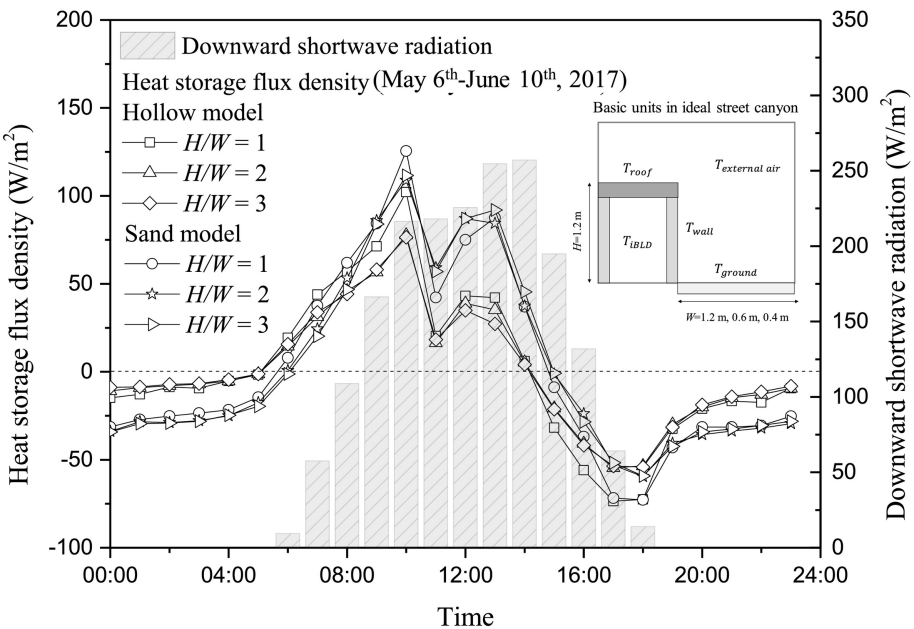

(d)

Figure 10cd